 doi:10.20944/preprints202201.0037.v1

Article

Broad-spectrum antimicrobial ZnMintPc encapsulated in magnetic-nanocomposites with Graphene Oxide/MWCNTs based on bimodal action of Photodynamic and Photothermal effect

Coralia Fabiola Cuadrado[1], Antonio Díaz[2], Kleber Orlando Campaña[3], Eric Cardona Romani[4], Francisco Javier Quiroz[5], Stefania Nardecchia[6], Alexis Patrice Debut[7], Karla Vizuete[7], Dario Niebieskikwiat [8], Camilo Ernesto Ávila[9], Mateo Alejandro Salazar[9], Cristina Cecibel Garzón-Romero[9], Ailín Amira Blasco[9], Miryan Rosita Rivera[9], María Paulina Romero [1,3].

[1] Departamento de Materiales, Facultad de Ingeniería Mecánica. Escuela Politécnica Nacional, Quito, Ecuador; coralia.cuadrado@epn.edu.ec; maria.romerom@epn.edu.ec
[2] School of Chemical Sciences and Engineering, Yachay Tech University, Urcuquí 100119, Ecuador; adiaz@yachaytech.edu.ec
[3] Laboratorio de Nuevos Materiales, Departamento de Materiales, Facultad de Ingeniería Mecánica. Escuela Politécnica Nacional, Quito, Ecuador; kleber.campana@epn.edu.ec; maria.romerom@epn.edu.ec
[4] Departamento de Física. Pontificia Universidad Católica de Río de Janeiro, Rio de Janeiro, Brasil; eric-takezo@gmail.com
[5] Departamento de Ciencia de Alimentos y Biotecnología DECAB. Escuela Politécnica Nacional, Quito, Ecuador; francisco.quiroz@epn.edu.ec
[6] Magnetic Soft Matter Group, Department of Applied Physics, Faculty of Sciences, University of Granada, C/Fuentenueva s/n, 18071 Granada, Spain; stefanianardecchia@yahoo.it
[7] Centro de Nanociencia y Nanotecnología, Universidad de Las Fuerzas Armadas ESPE, Av. Gral. Rumiñahui S/n, Sangolquí, P.O. BOX 171-5-231B, Ecuador; apdebut@espe.edu.ec; ksvizuete@gmail.com
[8] Colegio de Ciencias e Ingeniería, Universidad San Francisco de Quito, Quito, Ecuador; dniebieskikwiat@usfq.edu.ec
[9] Laboratorio de Investigación en Citogenética y Biomoléculas de Anfibios (LICBA), Centro de Investigación para la Salud en América Latina-CISeAL, Facultad de Ciencias Exactas y Naturales, Pontificia Universidad Católica del Ecuador, Av. 12 de octubre 1076 Apartado: 17-01-2184 Quito – Ecuador; camoavila@gmail.com; massuno@hotmail.com; ccgarzonrom@outlook.com; ailin.blasco.z@gmail.com; mriverai@puce.edu.ec
* Correspondence: coralia.cuadrado@epn.edu.ec; Tel.: +593987526539

Abstract: Microbial diseases have been declared one of the main threats to humanity, which is why, in recent years, great interest has been generated in the development of nanocomposites with antimicrobial capacity. In the present work, two magnetic nanocomposites, based on Graphene Oxide (GO) and Multiwall Carbon Nanotubes (MWCNTs) were studied. The synthesis of these magnetic nanocomposites consisted of three phases: first, the synthesis of Iron Magnetic Nanoparticles (MNPs) was carried out in the presence of MWCNTs and GO using the Co-precipitation method. The second phase consisted of the adsorption of photosensitizer menthol-Zinc phthalocyanine (ZnMintPc) into MWCNTs and GO, and the third phase was the encapsulation in poly (N-vinylcaprolactam-co-poly(ethylene glycol diacrylate)) poly (VCL-co-PEGDA) polymer VCL/PEGDA a biocompatible hydrogel, in order to obtain the magnetic nanocomposites: VCL/PEGDA-MNPs-MWCNTs-ZnMintPc and VCL/PEGDA-MNPs-GO-ZnMintPc. In vitro studies were carried out using *Escherichia coli* and *Staphylococcus aureus* bacteria and the *Candida albicans* yeast based on the PTT/PDT effect. This research describes the optical, morphological, magnetic and photophysical characterizations of nanocomposites and their application as antimicrobial agents. It was evaluated the antimicrobial effect of magnetics nanocomposites based on the Photodynamic/Photothermal (PDT/PTT) effect; for this purpose, doses of 65 mW cm^{-2} at 630 nm of light were used. The VCL/PEGDA-MNPs-GO-ZnMintPc nanocomposite was able to eliminate colonies of *E. coli* and *S. aureus*, while VCL/PEGDA-MNPs-MWCNTs-ZnMintPc nanocomposite was able to eliminate the three types of microorganisms; consequently, the latter is considered a broad-spectrum of antimicrobial agent in PDT and PTT.

Preprints (www.preprints.org) | NOT PEER-REVIEWED | Posted: 5 January 2022 doi:10.20944/preprints202201.0037.v1

Keywords: Antimicrobial nanomaterials, Carbon Nanotubes, Graphene, Magnetic Nanoparticles, hydrogel, Photodynamic Therapy, Photothermal Therapy, Nanocarrier.

Graphical Abstract:

53

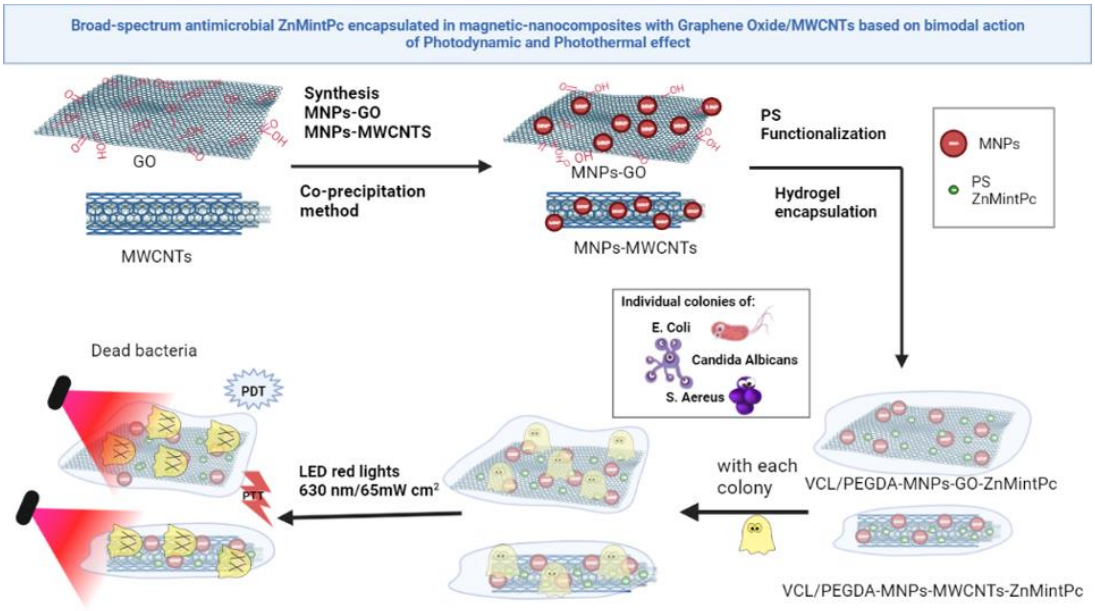

1. Introduction

Due to the COVID-19 pandemic, the study of microorganisms has increased substantially due to their ability to spread rapidly and adapt to different environments, for this reason the World Health Organization has declared microbial diseases as one of the main threats for humanity [1]. Currently, there are antibiotic therapies that help fight infections caused by microorganisms such as *Klebsiella pneumoniae, Escherichia coli, Staphlylococcus aureus, Neisseria gonorrhoeae* among others, but these have been losing their efficacy, which is why the development of new treatments is necessary [2].The generation of new nanocomposites that help to eliminate microorganisms provides a new alternative for the fight against infections caused by these pathogens [3].

Nanotechnology for the control of infectious diseases includes several strategies such as: the use of metal oxides for the generation of reactive oxygen species (ROS) , nanocomposites capable of damaging the membrane integrity or causing physical damage to the bacterial wall [4] and even inhibiting DNA replication and ATP production in cells [5] and use of Graphene-family materials for the microbial elimination [6–8]. In this regard, Romero et al., 2020 showed the ability of GO as an antimicrobial agent to eliminate *E. coli* and *S. aureus* bacteria through the combination of Photodynamic Therapy (PDT) and Photothermic Therapy (PTT) [9]. Peng et al, 2020 present a conjugated oligomer with antibacterial capacity to eliminate *E. coli* by PDT / PTT [10]. Xu et al., 2019 showed that nanocomposites based on Graphene and carbon nanotubes are capable of eliminating bacterial loads from Cyanobacteria, *E. coli, S. aureus, Pseudomonas aeruginosa, Bacillus subtilis, Pseudomonas putida* and *Rhodococcus spp*, based on the combination of PDT and PTT [11].

Photodynamic Therapy (PDT) is well known and studied for its use in cancer treatments, producing a minimum of side effects compared to other treatments used for cancer. PDT is an attractive operating modality based on the interaction of light with a photosensitizer (PS) and oxygen, thus producing reactive oxygen species (ROS) and free radicals capable of causing cell and microorganisms death with low toxicity [12–14]. This therapy has been used to treat skin diseases and some types of cancer such as: prostate, neck, lung, breasts, bladder, among others. [15–18].

 doi:10.20944/preprints202201.0037.v1

PS generally are classified by their activation wavelength, duration, and tissue penetration. One of the most widely used PS in PDT are the second generation, due to the photophysical and photochemical properties they possess, within this group are phthalocyanines, chlorins and benzoporphyrins [19,20]. Phthalocyanines (Pcs), are hydrophobic compounds whose activation wavelengths of 650 and 700 nm, allow deep tissue penetration. Pc reaches a high concentration in tumor tissue after 1 to 3 hours of its administration, and they are generally used to treat skin and subcutaneous lesions [21].

Zinc Menthol-Phthalocyanine (ZnMintPc) is a hydrophobic drug derived from phthalocyanine, whose structure is based on porphyrins but with a central Zinc atom and four methoxy groups around it that allow PS to be soluble in certain organic solvents [22]. The use of ZnMintPc has been limited due to its hydrophobic nature. Pcs can be soluble in aqueous media when encapsulated by hydrogels [23–25]. Pcs can also be combined with Nanoparticles (Np) to create hybrid nanostructures that increase the quantum yield of singlet oxygen, cell uptake, and their therapeutic effectiveness [26].

Due to the hydrophobic nature of PS, several types of nanocarriers have been studied that prevent them from adding to each other and losing their physico-chemical characteristics. [15,27,28]. Among these nanocarriers are carbon nanostructures such as: carbon nanotubes [29–31], graphene [27], and fullerenes [15,32,33] among others. These functionalized nanocarriers have excellent optical and mechanical properties, biocompatibility, and low toxicity. In addition to having other applications in nanomedicine such as immunotherapy, imaging, and the development of vaccines. [34–37].

Carbon Nanotubes (CNTs) were discovered by Iijima in 1991 [38] and consist of quasi one-dimensional structures formed by several layers of graphene rolled-up coaxially to form the tubes . They are classified into two types: with a single layer known as Single Wall Carbon Nanotubes (SWCNTs) and with several layers known as Multi-Wall Carbon Nanotubes (MWCNTs) [39,40]. CNTs possess great optical, electrical, thermal, physical, and kinetic properties, and excellent permeability in cells. For this reason, nanomedicine has put a lot of interest in their application as a drug transport systems, electrochemical biosensors, and biological markers, among others [41,42].

CNTs have been used as biosensors, biomarkers and drug transporters with a high carrying capacity [43,44]. To improve the effectiveness of their action, hybrid compounds have been created, that is, proteins, polymers, cell recognition ligands, nanoparticles, hydrophilic coatings have been incorporated into these structures, which provide them of new functions such as cell recognition, controlled drug release, avoiding aggregations in aqueous media, targeted transport, etc. [45–47].

Graphene is a two-dimensional nanostructure with sp^2 hybridization and strongly cohesive carbons, which gives the structure excellent properties: optical, electronic, mechanical and chemical which varies depending on its lateral size [48]. Graphene is known as a material with very high resistance and, hardness, it is light, has low toxicity and high flexibility, which makes it an innovative material in the fields of industry, construction, technology, medicine, and more [35,49,50]. Because of its excellent physicochemical characteristics, graphene has been used in the biomedical field to make biosensors, drug delivery systems antibacterial agents, for early detection of cancer, gene therapy, cancer cell imaging/mapping, among others [51].

In recent years, a great interest has arisen in the synthesis of magnetic nanoparticles since, thanks to their unique physicochemical properties, they can be used in PPT / PDT [52], drug delivery, theranostics, and others [53–55]. MNPs such as magnetite and hematite obtained from iron oxides are widely used in biomedicine, because they do not present cytotoxicity at low concentrations and are biocompatible [56–58]. MNPs can be anchored to carbon structures to obtain drug nanocarriers and can be directed by an external magnetic field [59,60].

VCL/PEGDA is a biocompatible hydrogel that can be obtained by emulsion polymerization, this hydrogel is very promising since it responds to physiological changes in the

 doi:10.20944/preprints202201.0037.v1

temperature of the human body [61,62]. Therefore, it can be used as a drug delivery system since it is capable of encapsulating hydrophobic and hydrophilic agents. The study carried out by Romero et al., 2021 shows the sustained release capacity of the drug colchicine encapsulated in VCL/PEGDA [63].

In the PDT strategy, PS must meet specific requirements: they must be selective, disperse nicely in tissue, and their photostability time is adequate for the treatment. Due to these needs, in this work we develop two magnetic nanocarriers based on MWCNTs and GO materials. Both nanocarriers are decorated with Fe-MNPs, thus giving the compound superparamagnetic properties. These nanocarriers were functionalized with PS ZnMintPc, a drug used in Photodynamic Therapy. To solve the hydrophobicity problem, present in ZnMintPc and MWCNTs, which prevents their dispersion in aqueous media, it has been necessary to provide them with the lipophilic envelope VCL/PEGDA hydrogel. Finally, the antimicrobial effect of these nanocomposites was evaluated to eliminate the bacteria *S. aureus, E. coli, C. albicans* using the PDT/PTT strategy.

2. Materials and Methods

2.1. Materials

For the synthesis and functionalization process, the following were used: MWCNTs and GO were provided by the Van de Graff Laboratory, Department of Physics PUC-RIO-Brazil; Zinc Menthol-Phthalocyanine was provided by the Federal University of São Carlos-Brazil; $Fe(SO_4)\cdot 7H_2O$ and H_2SO_4 from MERCK; NH_4OH, 14.8N and N-N Dimethylformamide from Fisher Scientific; $Fe_2(SO_4)_3\cdot H_2O$ from Baker's Analyzed; HNO_3 from the Fermont trade company; saline solution (pH = 7) from the Fisiol UB and Tween80 from the Chemical House (Quito-Ecuador).

For the VCL/PEGDA hydrogel synthesis by emulsion polymerization, the following reagents were used: N-vinylcaprolactam (VCL; Sigma Aldrich, 98%), and Poly(ethylene glycol) diacrylate (PEGDA;Sigma Aldrich, Mn 250), initiator: ammonium persulfate (APS; FMC Corporation, > 99%). Emulsifier: sodiumdodecyl sulfate (SDS; STEOL®CS-230 Stepan). Buffer: sodium hydrogen carbonate (SigmaAldrich, ≥ 99.7%) used as provided.

For characterization of MNPs-MWCNTs and MNPs-GO, were carried out a FT-IR spectroscopy analysis in a JASCO FT/IR-4100 spectrometer (wavenumber range 7800 to 350 cm^{-1}, resolution of 0.7 cm^{-1}) and a Raman spectroscopy analysis in a HORIBA Raman spectrometer LabRAM HR Evolution, where the samples were excited with a 2.33 eV (532 nm).

Magnetization (M) measurements were carried out using a Quantum Design Versalab VSM magnetometer, in the temperature range between -210 and +60 °C with applied magnetic fields $\mu_0 H$ up to 3 T.

The stability over time of the PS carried by the magnetic nanocomposites was characterized by a UV-VIS spectroscopy analysis within a wavelength range of 280 to 780 nm (resolution better than1.8 Å), using a Thermo Scientific UV-VIS Spectrophotometer model Evolution 220. The DPBF photobleaching studies and thermic studies were carried out with a homemade equipment based on LED red light at 635 nm, 65.5 mW cm^{-2} and DPBF photobleaching study was characterized in a UV-VIS Specord 210 Plus. The XRD analysis was performed on a PANalytical brand EMPYREAN Diffractometer, operating in a θ-2θ configuration (Bragg-Brentano geometry) equipped with a copper X-ray tube (Kα radiation λ = 1.54056 Å) at 45 kV and 40 mA.

2.2. Methods

2.2.1 Morphological studies

The morphology and semiquantitative elemental composition were evaluated by Scanning Electron Microscopy (SEM) and Energy Dispersive X-ray Spectroscopy (EDS). For this, an aliquot of the sample was fixed to an aluminum sample holder using a double layer of carbon tape. These analyzes were carried out on the SEM Tescan, Mira 3 equipped

 doi:10.20944/preprints202201.0037.v1

with a Schottky field emitter. EDS was performed in the SEM chamber using a Bruker, X-Flash 6|30 detector with a resolution of 123 eV at Mn Kα.

For Transmission Electron Microscopy (TEM), the samples were dispersed in a BRANSON 1510 ultrasonic bath for 30 minutes. Next, approximately 5 µL of the sample was placed on a transmission electron microscope grid (formvar / carbon, 300 mesh) and the solvent was removed with filter paper. The samples were observed in the TEM FEI transmission electron microscope, Tecnai G2 Spirit Twin equipped with an Eagle 4k HR camera at 80 kV

For scanning transmission electron microscopy (STEM), 5 µL of the sample was placed on a transmission electron microscope grid (formvar / carbon, 300 mesh) and the solvent was removed with filter paper. Staining was performed with 1% Phosphotungstic Acid for 1 second for *S. aureus* and 1 minute for *E. coli*, the solvent was removed, and it was observed in the SEM Tescan, Mira 3 scanning electron microscope in transmission mode.

2.2.2. Synthesis of graphene oxide using the Hummers' method.

GO was prepared according to the Hummers' method[64]. Graphite powder with 99% purity was used for the synthesis of GO. Chemical products, including $NaNO_3$, $KMnO_4$, H_2SO_4, aqueous solutions of H_2O_2 and HCl, were purchased from Sigma Aldrich. The GO powder was obtained after lyophilization of the suspected GO in deionized water.

2.2.3. Purification of MWCNTs

The purification of the MWCNTs was carried out using an acid attack. 5.3 mg of MWCNTs were dispersed with 5% Tween 80 in 10mL of distilled water, stirred at 200 rpm for 24 hours to ensure that the MWCNTs were well dispersed. Then, in a solution of 4 mL of HNO_3 and 12 mL of H_2SO_4 (1: 3 ratio), the solution of MWCNTs previously treated was placed, allowed to cool and then stirred magnetically for 3 hours. Several washes of the MWCNTs were performed using 0.22 µm pore micropore filtration until a neutral pH was obtained.

2.2.4. Synthesis and Functionalization of MNPs-MWCNTs and MNPs-GO

In 18mL of pure water, the following were dispersed: purified MWCNTs, 225 mg of $FeSO_4$, 450 mg of (Fe_2 $(SO_4)_3$) and 5% Tween 80. This was placed under magnetic stirring for 3 hours and subsequently the sample was added carefully in 150 mL of NH_4OH. The mixture was exposed to magnetic stirring in an inert atmosphere for 1 hour at 200 rpm. Finally, several magnetic purifications of the MNPs-MWCNTs nanocarrier were carried out until the pH was neutralized and it was allowed to dry.

For the synthesis of MNPs-GO, the same process was used, but using 5.3 mg of GO instead of MWCNTs.

Also, as a control sample for the magnetic measurements, free-standing iron nanoparticles were prepared using the same co-precipitation method, but without GO or MWCNTs.

2.2.5. Synthesis of Polyethylene Glycol Diacrylate-Vinylcaprolactam (VCL/PEGDA)

The synthesis of the hydrogel was carried out by emulsion polymerization of 2 g of VCL, 0.08 g of PEGDA, STEOL CS-230 and 0.08 of NaHCO3 dispersed in 235 mL deionized water. The mixture was slowly placed in the chemical reactor with stirring at 350 rpm and at a temperature of 70 °C, maintaining a stream of Nitrogen for one hour. Then the initiator (0.03 g of Ammonium Persulfate dissolved in 15 mL of distilled water) was added to the solution and the reaction was kept at 70 °C for 7 hours. After this time, the mixture was allowed to cool under stirring at 200 rpm and 25 °C to avoid aggregation for 12 hours. Finally, the hydrogel obtained was dialyzed against DDI water to remove impurities and unreacted reagents [63].

2.2.6. Functionalization of MNPs-MWCNTs; MNPs-GO with ZnMintPc in the presence of VCL/PEGDA

In 10mL of pure water, 2 mg of MNPs-MWCNTs were dispersed with 5% Tween and it was stirred magnetically for 24 hours at 200rpm, then it was placed in sonication for 30 minutes. 10 mL of VCL/PEGDA was added to the mixture and it was stirred magnetically for 4 hours at 200rpm.

Within the 20 mL of the VCL/PEGDA-MNPs-MWCNTs solution, 0.67 mL of ZnMintPc solution (0.25 mM) were added, after which the mixture was sonicated for 4 hours at 250 rpm. The solution was covered with aluminum foil to avoid ZnMintPc photodegradation produced by light exposure.

The same process was carried out with MNPs-GO, obtaining the VCL/PEGDA-MNPs-GO nanocomposite.aue

2.2.7. Quenching Experiment of 1,3-Diphenyl Isobenzofuran

The fluorescence and absorption characteristics of 1,3-diphenylisobenzofuran (DPBF), a singlet oxygen trapping chemical, are widely employed to detect and quantify singlet oxygen [65]. This agent has an absorption range within 410-420 nm, emitting blue fluorescence. When DPBF interacts with oxygen, it produces o-dibenzoylbenzene, which does not absorb visible light. The amount of $^1O_2$ produced is shown by a reduction in DPBF absorbance [9]. 5 mg of DPBF was dispersed in 1 mL of DMF to later disperse it in the solutions with nanocomposites.

For this experiment, first, a UV-VIS SPECORD 210 Plus spectrophotometer (resolution of 2.3-2.5 nm) in a range of 300 to 800 nm was used, a reference solution was prepared with 10 mL of deionized water and 10% Tween 80. Then in 3 mL of this reference solution 100 µL of VCL/PEGDA-MNPs-GO (0.1 mg/mL) was added. The same process was repeated with the nanocomposites VCL/PEGDA-MNPs-MWCNTs (0.1mg/mL), VCL/PEGDA-MNPs-MWCNTs-ZnMintPc (0.1 mg/mL) and VCL/PEGDA-MNPs-GO-ZnMintPc (0.1 mg/mL). After that, 20 µL of the DPBF (18.5 mM) solution was placed on each of them and they proceeded to irradiate at different times to observe the decrease in absorbance of the band found at 418 nm from DPBF.

2.2.8. Thermal Studies

The thermal studies were carried out by irradiating with a red light of 630 nm, 65.5 mW cm^{-2} to deionized water, VCL/PEGDA, MNPs, GO, MWCNTs, VCL/PEGDA-MNPs-GO and VCL/PEGDA-MNPs-MWCNTs, taking the temperature every 5 to 10 minutes until the temperature of the samples does not change.

2.2.9. Antimicrobial Studies

For the antimicrobial study was used cryovials with the microorganisms: *Staphylococcus aureus* ATCC: 25923, *Escherichia coli* ATCC: 25922 and *Candida albicans.* They were thawed at room temperature, and the content was inoculated in Mueller-Hinton broth (Difco™). The culture medium was incubated overnight at 37 °C. After this period, the absorbance of each medium was determined by spectrophotometry (Thermo Scientific ™ Orion ™ AquaMate 8000 UV-Vis) and diluted in Mueller-Hinton broth to reach the concentration established for the bioassays: 10^7 CFUs mL^{-1} for *E. coli*, 10^6 CFUs mL^{-1} for *S. aureus*, and 10^5 CFUs mL^{-1} for *C. albicans*.

Upon reaching the indicated concentration, each medium was dispensed into microtubes as follows: 6 aliquots of 1 mL per magnetic nanocomposites (VCL/PEGDA-MNPs-GO-ZnMintPc, VCL/PEGDA-MNPs-MWCNTs-ZnMintPc, VCL/PEGDA-MNPs-GO and VCL/PEGDA-MNPs-MWCNTs) and 6 aliquots of 1 mL as control. Half of the aliquots were used to evaluate the activity of the magnetics nanocomposites under light irradiation, while the other half was not exposed to these conditions.

The microtubes were centrifuged at 3000 rpm for 10 min. The supernatant was discarded, and 1 mL of PBS was added to wash the cells and remove the remains of the culture medium. The pellet was resuspended and recentrifuged under the same conditions. PBS

 doi:10.20944/preprints202201.0037.v1

was discarded and 1 mL of the compound was dispensed into each microtube; in the control microtubes the cells were resuspended again with PBS. Each tube was vortexed to dissolve the pellet again and incubated at 37 °C in the dark for 45 minutes.

At the end of the incubation period, 3 aliquots of each compound and 3 controls were subjected to light irradiation using a red light of 630 nm, 65.5 mW cm^{-2}. The remaining tubes were not irradiated.

Serial dilutions of each aliquot were made in PBS. 4 µL of each dilution was inoculated into an 8-part Petri dish with Mueller-Hinton agar (Difco™). Each inoculum was streaked for colony isolation. Petri dishes were incubated for 24 h at 37 °C, and after this period the number of colonies was counted per dilution.

3. Results

3.2. Composition and structure characterization of magnetic nanocomposites

A FT-IR spectroscopy was performed on the magnetics nanocomposites to study the difference in oxygen-related functional groups (Figure 1). Figure a shows the FT-IR spectra of MNPs-MWCNTs, which presents characteristic bands. The band at 3373 cm^{-1} is attributed to the vibration of the hydroxyl group (OH), the 1636 cm^{-1} band, to the stretching of the C=O group, which indicates that MWCNTs are linked to MNPs through hydrogen bonds. Additionally, other bands appear in the range 1400-1730 cm^{-1}, that corresponds to the OH-C=O, -COO, -COOH groups that have been added due to acid treatment and functionalization with MNPs [66–68]. Finally, the characteristic bands of the MNPs appear at 709 and 623 cm^{-1}, which indicate the stretching vibration of Fe-O-Fe characteristic of Fe-MNPs [69].

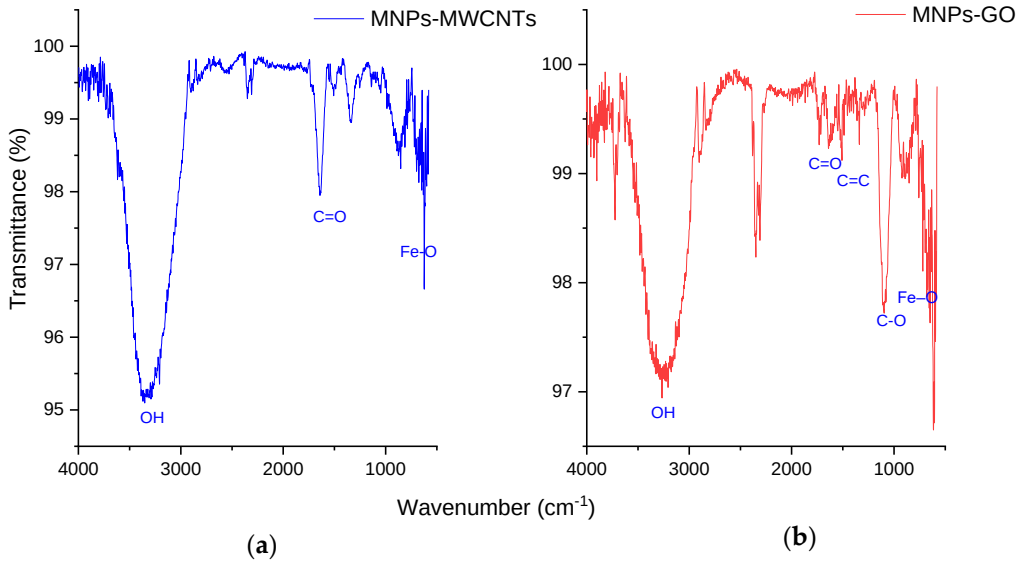

Figure 1. FT-IR spectra: (**a**) MNPs-MWCNTs; (**b**) MNPs-GO.

Error! Reference source not found.1b presents the FT-IR spectra of the MNPs-GO nanocarrier where characteristic bands of GO are identified, within which there is a band around 3327 cm^{-1} corresponding to the bending and vibration of the OH stretching of the C- groups. The band at 1636 cm^{-1} corresponds to the vibration of the C=C, the bands around 800 cm^{-1} and 1269 cm^{-1} correspond to the epoxy group, bands at 1342 cm^{-1}, 1247 cm^{-1}, 1049 cm^{-1} correspond to the stretching vibration of the carboxy groups C-O, C-C-O and alkoxy C-O respectively[70].

Preprints (www.preprints.org) | NOT PEER-REVIEWED | Posted: 5 January 2022 doi:10.20944/preprints202201.0037.v1

The 622 cm^{-1} band is attributed to the vibrational stretching of the Fe-O group that must be anchored to the COO group. Some of the bands close to 1000 cm^{-1} may be related to deformation vibrations of the metal -OH bond, that is, related to the Fe-OH group [71].

Figure **2**2a shows the Raman spectra of not purified MWCNTs (Fig. 2a), purified MWCNTs (Fig. 2b) and MNPs-MWCNTs (Fig. 2c). These spectra show characteristic bands of the MWCNTs: band D or band of defects and the first and second-order bands G and 2D respectively. D-band is at 1337 cm^{-1} and corresponds to the presence of defects in the graphite, which means the presence of multiple carbon sheets that are not directly aligned sheet to sheet, which induces a loss of translational symmetry in the two-dimensional network. Due to the same effect, a secondary phonon is produced that gives rise to the presence of the G-band at 1566 cm^{-1}. The fundamental band G is a tangential elongation band that is attributed to the in-plane vibration of the C-C bond and is typical of carbon-derived materials [72–75]. It is observed that $\frac{I_D}{I_G}$ ratio increases in the treated MWCNTs spectra compared to the untreated MWCNTs spectra, this occurs because the acid treatment causes some bonds to be broken and functional groups are formed that later serve for functionalization with the MNPs, when observing the presence of the three bands, it shows us that the MWCNTs are maintained. Comparing $\frac{I_D}{I_G}$ ratio of treated MWCNTs spectra with the MNPs-MWCNTs, the last one increases because the structure of the MWCNTs have been functionalized with the MNPs creating a defective graphite structure, as it is observed that the characteristic bands of Fe-MNPs are manifested in 210 and 273 cm^{-1} [76].

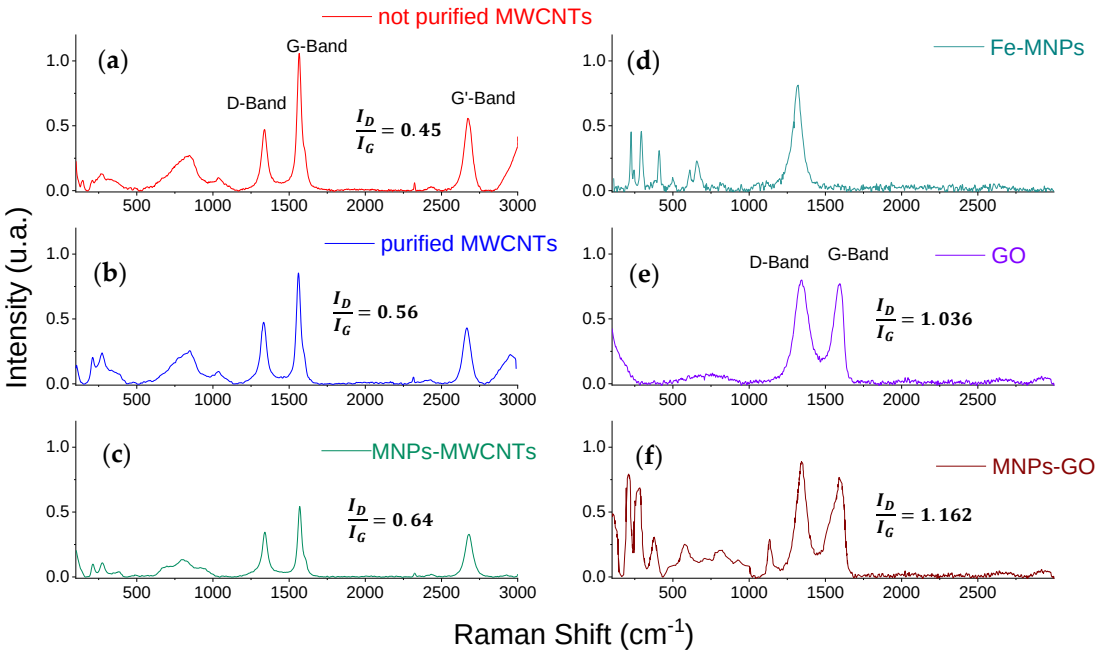

Figure 2. Raman Spectra: (**a**) not purified MWCNTs, (**b**) Purified MWCNTs, (**c**) MNPs-MWCNTs; (**d**) Fe-MNPs; (**e**). GO; (**f**) MNPs-GO; $E_{láser}$=2.33eV, λ=532 nm.

In **Error! Reference source not found.**2c we can find the Raman spectra of Fe-MNPs with its characteristic bands a: 224, 296 (Eg), 408 (Eg), 612 (Eg), 658 and 1320 cm^{-1} [77,78]. In **Error! Reference source not found.**2e we find the characteristic bands of GO: an intense D band at 1340 cm^{-1}, a G-phase vibration band at 1589 cm^{-1} and the D + D′ band located around 2900 cm^{-1} which is activated by defects and appears with the combination of phonons with different linear moments around points K and Γ in the Brilloüin zone [79,80]. The relationship of the D and G bands allows us to determine the degree of disorder of

the carbon structure in the GO the $\frac{I_D}{I_G}$ =1.036 ratio due to the presence of the Carboxyl groups at its ends. In **Error! Reference source not found.**2f we can observe the MNPs-GO nanocomposite where there is a shift of the bands due to the fact that the nature of iron oxide when combined with carbon nanostructures can affect the spectral position and amplification of the phonon peaks [81], but the GO bands are in the same position with the difference that now the $\frac{I_D}{I_G}$ ratio is 1.162, which indicates that the MNPs-GO is a slightly more disordered structure than the GO which may be due to the anchoring of Fe-MNPs functional groups to GO [82].

3.2. *Magnetic properties*

We studied the magnetic properties of three samples: the nanocomposites VCL/PEGDA-MNPs-MWCNTs and VCL/PEGDA-MNPs-GO and, for comparison, the free-standing iron nanoparticles (MNPs). All the studied samples present the typical ferromagnetic (FM) behavior of the Fe nanoparticles, with a very small coercivity of less than 2 mT at room temperature (less than 5 mT at T = -210 °C). This small coercivity indicates that the MNPs are not directly attached to the carbon structures, since in that case large coercivities of hundreds of mT have been observed [83,84] . In our case, according to the FT-IR spectroscopy results in section 3.1., the link between the MNPs and the C atoms appears to be mediated by hydrogen bonds, thus reducing the Fe-C magnetic coupling. In figure 3a we show some representative M vs H loops measured at two different temperatures, -210 °C and +20 °C, for the three samples. From these curves, we obtained the saturation magnetization (M_S) as a function of temperature by means of the usual law of approach to saturation (LAS) [85–87], given by:

$$M(H) = M_S\left(1 - \frac{a}{H} - \frac{b}{H^2}\right) + \chi H, \quad (1)$$

In this equation a and b are constants, and the last term accounts for the non-ferromagnetic contributions, such as the disordered shell of the nanoparticles. The last is valid only at high fields, close to saturation, thus we used it to fit our $M(H)$ curves for applied fields between 1 and 3 T, as exemplified by the solid lines in figure 3a for T = -210 °C. From these fits, we obtained M_S at several temperatures between -210°C and +60°C (see figure 3b). In the case of the VCL-PEGDA-MNPs-MWCNTs and VCL-PEGDA-MNPs-GO samples, the value of the magnetization appears substantially reduced, since most of the mass (>98%) corresponds to the hydrogel. Therefore, in order to directly compare the measured magnetic moment with that of pure iron, the value of the saturation magnetization was corrected by the mass fraction of nanoparticles, x = 1.43% for the VCL-PEGDA-MNPs-MWCNTs sample and x = 1.37% for the VCL-PEGDA-MNPs-GO sample.

Preprints (www.preprints.org) | NOT PEER-REVIEWED | Posted: 5 January 2022 doi:10.20944/preprints202201.0037.v1

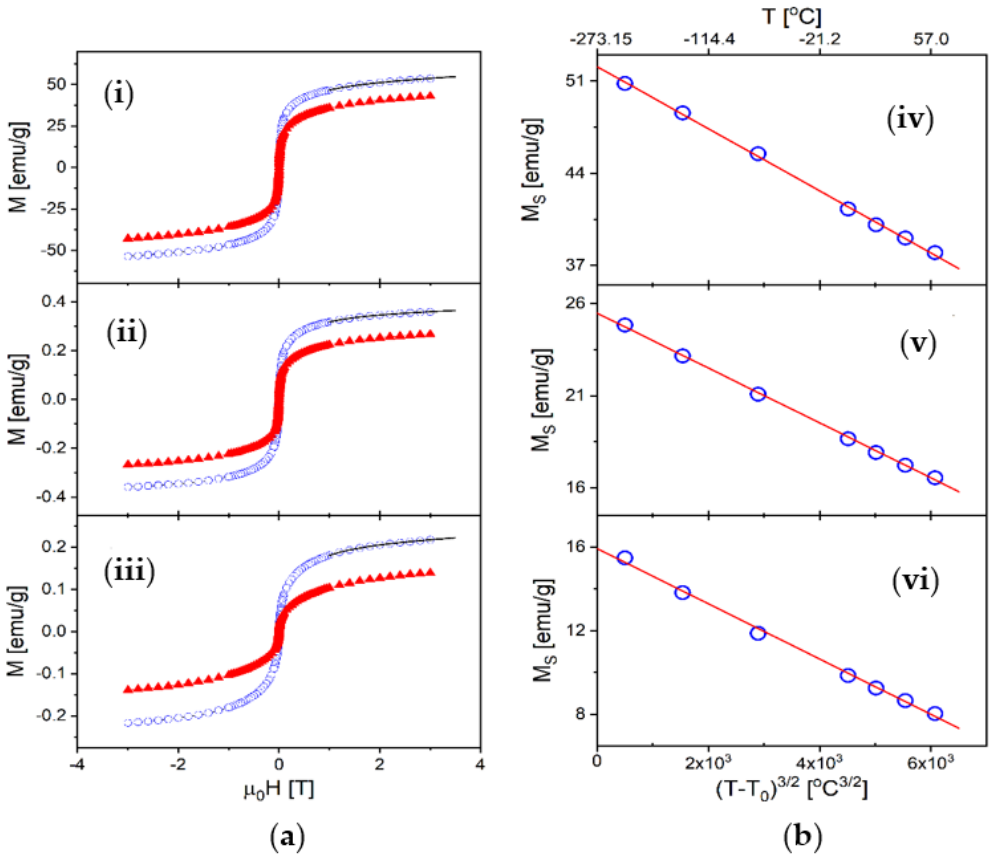

Figure 3. (**a**) Magnetization vs applied magnetic field: (**i**) the free-standing nanoparticles, (**ii**) VCL-PEGDA-MNPs-MWCNTs and (**iii**) VCL-PEGDA-MNPs-GO. The curves shown were measured at two different temperatures, T = -210°C (circles) and T = 20°C (triangles). The solid lines are examples of the fit of the data using the law of approach to saturation (LAS) of Eq. (1); (**b**) Saturation magnetization as a function of temperature: (**iv**) the free-standing nanoparticles, (**v**) VCL-PEGDA-MNPs-MWCNTs and (**vi**) VCL-PEGDA-MNPs-GO. The solid lines match the data showing that MS follows the Bloch´s law given by Eq. (2).

The saturation magnetization as a function of temperature is presented in figure 3b, where we also show that, for all three samples, M_S closely follows the well-known Bloch's law for FM nanoparticles [88–90],

$$M_S(T) = M_0 \times \left[1 - B\,(T - T_0)^{\frac{3}{2}}\right], \quad (2)$$

where M_0 is the saturation magnetization at the temperature of the absolute zero degrees Kelvin (T_0 = -273.15 °C), and B is the so-called spin-wave constant. The results for these magnetic parameters are presented in table 1. The values obtained for B are indeed very similar to those measured in other Fe-nanoparticles systems, [89,90] $B \sim 10^{-5}$-10^{-4} °C$^{-3/2}$, implying the existence of comparable thermally induced magnetic excitations within the FM volume. On the other hand, our results show that the saturation magnetization is in all cases much smaller than that of pure iron, M_{Fe} = 222 emu g^{-1}. However, in the case of the free-standing nanoparticles, M_S remains larger than for the nanoparticles submerged within the hydrogel, indicating that the size of the non-FM (disordered) shell increases in the presence of the gel medium. Moreover, the difference between the samples becomes even deeper at room temperature, where the saturation magnetization decreases due to thermal effects (see table 1). From this analysis, the effective FM volume (the size of the FM core of the nanoparticles) can be estimated by comparing M_0 with M_{Fe}, such that the fraction of the nanoparticle volume that remains FM can be estimated as

 doi:10.20944/preprints202201.0037.v1

$$f = \frac{M_0}{M_{Fe}}, \quad (3)$$

The very small FM volume fraction in the case of the VCL-PEGDA-MNPs-MWCNTs and VCL-PEGDA-MNPs-GO samples likely indicates that the presence of the hydrogel induces a strong oxidation of the surface of the nanoparticles, or some interdiffusion that corrodes the surface and reduces the magnetic moment. Moreover, the larger value of the spin-wave constant in these two samples is consistent with a more significant influence of surface effects [90], which produce a faster decrease of the saturation magnetization when the temperature increases.

Table 1. Magnetic parameters for the three studied samples: saturation magnetization at T_0=- 273.15°C (M_0), saturation magnetization M_s at 20°C, a fraction of the volume of the nanoparticles that remain ferromagnetic (f), and spin-wave constant (B).

Sample	M_0 (emu g^{-1})	M_s @ 20 °C (emu g^{-1})	f (%)	B (°C$^{-3/2}$)
MNPs	52.1	40.1	23.5	4.5 x 10^{-5}
VCL-PEGDA-MNPs-MWCNTs	25.5	17.9	11.5	5.8 x 10^{-5}
VCL-PEGDA-MNPs-GO	15.9	9.3	7.2	8.3 x 10^{-5}

3.3. *Optical Properties of Magnetic Nanocomposites*

UV-VIS absorbance spectra and the photoluminescence emission were obtained. In Support information (S1a, S1b and S1d) we show the ZnMintPc-DMF and the nanocomposites: VCL/PEGDA-ZnMintPc and VCL/PEGDA-MNPs-MWCNTs-ZnMintPc respectively. We observe the presence of bands at 354 nm (Band of B or Soret), 616 nm, and at 684 nm (Band Q), characteristic of the absorption spectra of ZnMintPc.

Furthermore, it can be seen that as the concentration of ZnMintPc increases, the absorption of the B and Q bands increases proportionally without their dislocation. This allows us to conclude that the Beer-Lambert law is fulfilled and there is no drug aggregation, indicating that N,N-Dimetilformamida (DMF) is a good solvent for this PS [91,92]. Furthermore, it is also concluded that the VCL-PEGDA hydrogel disperses PS similarly to DMF. In Support Information (S1c, S1d) the UV-VIS spectra of nanocomposites based on MNPs-MWCNTs (VCL-PEGDA-MNPs-MWCNTs and VCL-PEGDA-MNPs-MWCNTs-ZnMintPc) are presented, where the band corresponding to MWCNTS at 265 nm cannot be visualized [93] but the representative band of Fe-MNPs can observed at 315 nm.

Figure S2a in support Information shows the UV-VIS spectra of MNPs-GO. The band corresponding to GO at 230 nm cannot be visualized [94–96]. The less intense bands correspond to Fe-MNPs appear at 315 and 336 nm. The latter band has undergone a hypsochromic shift due to functionalization with both MWCNTs and GO in the presence of an organic solvent (ammonium hydroxide used for MNPs syntheses) [97,98].

The calibration curve of figure 4a was obtained from the Q band found at 684 nm belonging to ZnMintPc and described in S1 and S2, which is in a region of the spectra of interest for treatment in PDT. It can be observed that the higher the concentration of ZnMintPc in the nanocomposites (VCL-PEGDA-ZnMintPc, VCL-PEGDA-MNPs-GO-ZnMintPc and VCL- PEGDA-MNPs-MWCNTs-ZnMintPc), the greater the intensity of the 684nm band; but when comparing with the ZnMintPc dispersed in DMF, the latter shows the highest intensity in relation to all nanocomposites. This indicates that the VCL-PEGDA hydrogel adequately disperses the hydrophobic ZnMintPc PS in an aqueous solution [99–101]. It can be seen that the 684 nm absorption band of ZnMintPc (0.52 μM) decreases as the number of functionalized components increases, as presented in 4b. The percentage of decrease for VCL/PEGDA-MNPs-MWCNTs-ZnMintPc nanocomposites is 38.2% and for VCL/PEGDA-MNPs-GO-ZnMintPc it is 35.54%.

 doi:10.20944/preprints202201.0037.v1

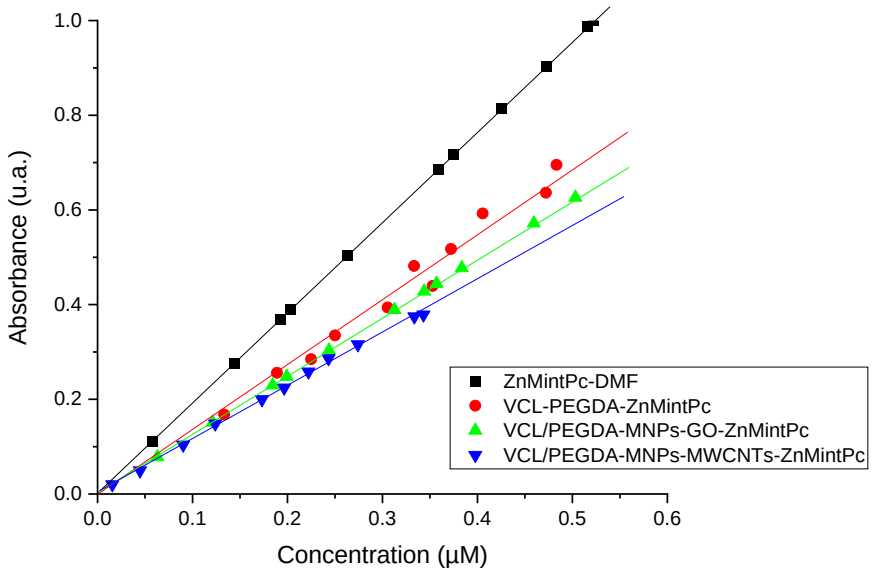

(**a**)

	Absorbance
ZnMintPc-DMF	100%
VCL/PEGDA-ZnMintPc	71.47%
VCL/PEGDA-MNPs-GO-ZnMintPc	64.46%
VCL/PEGDA-MNPs-MWCNTs-ZnMintPc	61.73%

(**b**)

Figure 4. (**a**) Composites calibration curve of ZnMintPc (0.52 μM) from: PS in DMF, VCL/PEGDA, VCL/PEGDA-MNPs-GO and VCL/PEGDA-MNPs-MWCNTs; (**b**) Absorbance of ZnMintPc-DMF and nanocomposites.

The temporal stability study observed in Figure 5 was carried out during the first three hours after having functionalized the PS with the nanocarrier (VCL/PEGDA-MNPs-MWCNTs-ZnMintPc or VCL/PEGDA-MNPs-GO-ZnMintPc) and one day after. It can be seen that in both cases, as time passes, the intensity of band B increases, while the intensity of band Q decreases. This phenomenon is because the PS begins to photobleached, without showing aggregation of nanocomposites for 24 hours.

Preprints (www.preprints.org) | NOT PEER-REVIEWED | Posted: 5 January 2022 doi:10.20944/preprints202201.0037.v1

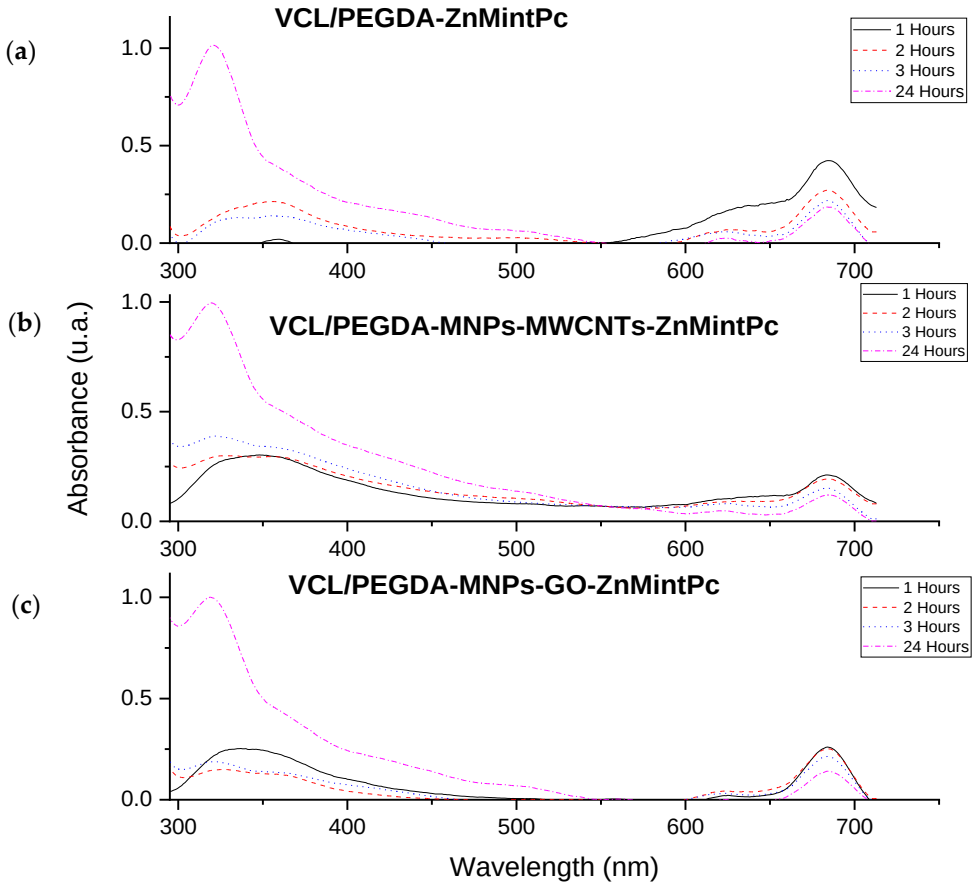

Figure 5. Stability curves over time for the: (**a**) VCL-PEGDA-ZnMintPc; (**b**) VCL/PEGDA-MNPs-MWCNTs-ZnMintPc and (**c**) VCL/PEGDA-MNPs-GO-ZnMintPc; ZnMintPc =0.27μM

The stability over time (Figure 6a) indicates that the intensity of PS decays exponentially as time passes. The nanocomposites were evaluated during 24 hours and it was found that when functionalized with nanocarriers based on MWCNTs and others based on GO the speed of the decay of the PS is less compared to the PS in the hydrogel. Figure 6b shows the percentage of decay over time of each nanocomposite, where-in two hours the nanocomposites based on GO and MWCNTs have PS decays of only 2.98% and 8.83% respectively, while for VCL/PEGDA-ZnMintPc (with no carbon nanocomposites) the decay rate is much higher, 35.87%. After 24 hours nanocomposites based on GO and MWCNTs have only allowed the PS to decline to the 50% range, while with only the hydrogel, it declined to 43.76%, which is why it can be said that VCL/PEGDA-MNPs-GO-ZnMintPc and VCL/PEGDA-MNPs-MWCNTs-ZnMintPc increase the photobleaching time of the PS.

Preprints (www.preprints.org) | NOT PEER-REVIEWED | Posted: 5 January 2022 doi:10.20944/preprints202201.0037.v1

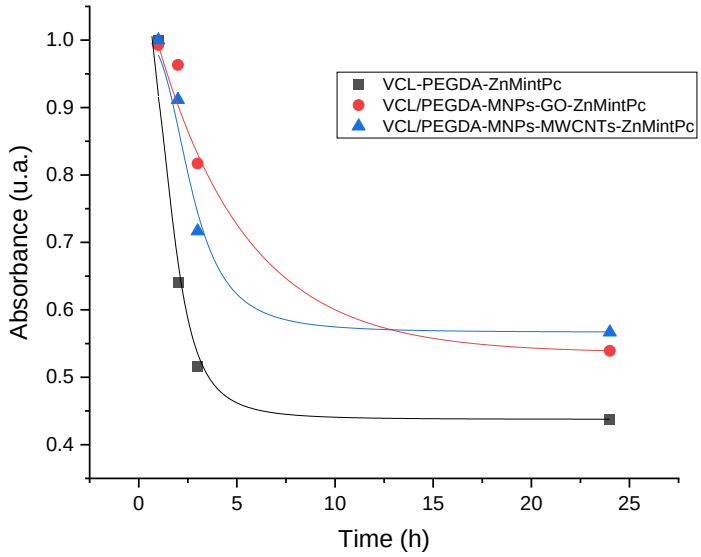

(**a**)

Time (h)	VCL-PEGDA-ZnMintPc	VCL/PEGDA-MNPs-GO-ZnMintPc	VCL/PEGDA-MNPs-MWCNTs-ZnMintPc
1	100%	100%	100%
2	64.13%	97.02%	91.17%
3	51.55%	82.30%	71.68%
24	43.76%	54.33%	56.67%

(**b**)

Figure 6. (**a**) Decay curves of: VCL-PEGDA-ZnMintPc, VCL/PEGDA-MNPs-MWCNTs-ZnMintPc and VCL/PEGDA-MNPs-GO-ZnMintPc. ZnMintPc =0.27μM; (**b**) Decay of ZnMintPc in nanocomposites in 24 hours.

3.4. Photodynamic Analyses

DPBF photobleaching was performed in VCL/PEGDA-MNPs-GO, VCL/PEGDA-MNPs-MWCNTs, VCL/PEGDA-MNPs-GO-ZnMintPc and VCL/PEGDA-MNPs-MWCNTs-ZnMintPc, to evaluate the efficiency of singlet oxygen production of the nanocomposites using 630 nm light, with an intensity of 65.5 mW cm^{-2}. In Support Information (S3 and S4) it is possible to observe the decrease of the 418 nm DPBF band of each nanocomposite as a function of time. For the VCL/PEGDA-MNPs-GO and VCL/PEGDA-MNPs-MWCNTs nanocomposites, a slight decrease in the 418 nm band is observed at an irradiation time of 29 and 35 minutes respectively (S3a and S3b respectively). On the other hand, for nanocomposites with the presence of ZnMintPc (VCL/PEGDA-MNPs-GO-ZnMintPc and VCL/PEGDA-MNPs-MWCNTs-ZnMintPc), a rapid decay of the 418nm band is observed until all the DPBF present is photobleached in solution. This total photobleaching is observed in around 9 and 11 minutes of irradiation respectively.

For each nanocomposite, absorbance vs. photoirradiation curves were constructed. Taking the band of the 418 nm of DPBF, an exponential decay fit was made to get the decay time presented in figures 7a and figure 7b.

The decay times are different for the nanocomposites without ZnMintPc (VCL/PEGDA-MNPs-GO and VCL/PEGDA-MNPs-MWCNTs), the VCL/PEGDA-MNPs-

Preprints (www.preprints.org) | NOT PEER-REVIEWED | Posted: 5 January 2022 doi:10.20944/preprints202201.0037.v1

MWCNTs being larger 34700 ± 700 s, indicating a minor generation of $^1O_2$ by photooxidation of DBPF in relation to the GO nanocomposite. For nanocomposites with ZnMintPc (VCL/PEGDA-MNPs-GO-ZnMintPc and VCL/PEGDA-MNPs-MWCNTs-ZnMintPc), two decay times are obtained, one indicating a rapid decay to about 60 s photoirradiation and the second one, a slow decay to about 700 s photoirradiation. Once again, the slow decay gives a longer decay time for nanocomposites with MWCNTs (1140 ± 260 s) than GO nanocomposite.

The presence of ZnMintPc in the nanocomposites generates a rapid photooxidation of DPBF. Therefore, the results indicate that the photobleaching of DPBF is mainly due to PDT effects mediated by VCL/PEGDA-MNPs-GO-ZnMintPc and VCL/PEGDA-MNPs-MWCNTs-ZnMintPc nanocomposites, with the nanocomposite containing GO and the photosensitizing ZnMintPc exhibiting greater singlet oxygen generation.

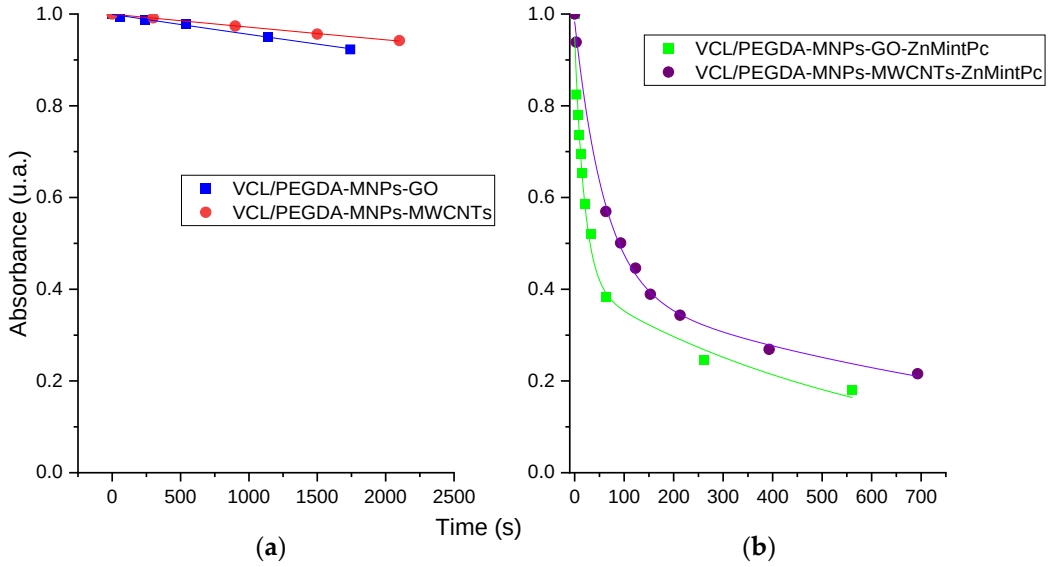

(**a**) (**b**)

VCL/PEGDA-MNPs-MWCNTs	VCL/PEGDA-MNPs-GO
34700 ± 700 s	22300 ± 900 s
VCL/PEGDA-MNPs-MWCNTs-ZnMintPc	**VCL/PEGDA-MNPs-GO-ZnMintPc**
1140 ± 260 s	630 ± 190 s

(**c**)

Figure 7. Decay curve of DPBF from: (**a**) VCL/PEGDA-MNPs-GO and VCL/PEGDA-MNPs-MWCNTs; (**b**) VCL/PEGDA-MNPs-GO-ZnMintPc and VCL/PEGDA-MNPs-MWCNTs-ZnMintPc; (**c**) Decay times of nanocomposites. DPBF = 18.5mM, GO = 3.47 μg mL^{-1}, MWCNTs = 3.47 μg mL^{-1}, MNPs= 93.3 μg mL^{-1} and ZnMintPc= 8.1 μM.

3.5. Thermal Studies

In the thermal study curves of figure 8, it can be observed that the MNPs, GO and MWCNTs solutions (blue, purple and light blue respectively) act as photothermic materials when irradiated with red light for about 100 minutes. They can reach temperatures between 50.8 to 54.8 °C, which makes them suitable for use in Photothermic Therapy for their ability to convert red and near-infrared light (NIR) into heat and to transport drugs as mentioned in the literature [52,102–105]. In the thermal curves of figure 8, it can also be observed that the nanocomposites containing the VCL-PEGDA hydrogel, such as pure

Preprints (www.preprints.org) | NOT PEER-REVIEWED | Posted: 5 January 2022 doi:10.20944/preprints202201.0037.v1

VCL/PEGDA, VCL/PEGDA-MNP-GO and VCL/PEGDA-MNP-MWCNTs when irradiated with red light for about 100 minutes; a slight decrease in temperature is observed in relation to the thermal curve of deionized water (reference). It is also observed that around 80 minutes of irradiation, all the curves have the same temperature reached by the deionized water curve (Figure 8b).

It can be observed that the MNPs, GO and MWCNTs solutions raise their temperature around 10°C in relation to the control (deionized water) and the VCL/PEGDA-MNP-GO and VCL/PEGDA-MNP-MWCNTs nanocomposites. It can be concluded that the VCL/PEGDA hydrogel acts as a kind of cooling liquid, this would be expected because its main components separately have good calorific capacities [106–108], therefore the hydrogel would inherit this property, which explains that the nanocomposites covered by hydrogel maintain a temperature similar to the temperature of the control solution (deionized water) at an irradiation time of more than 100 minutes with red light.

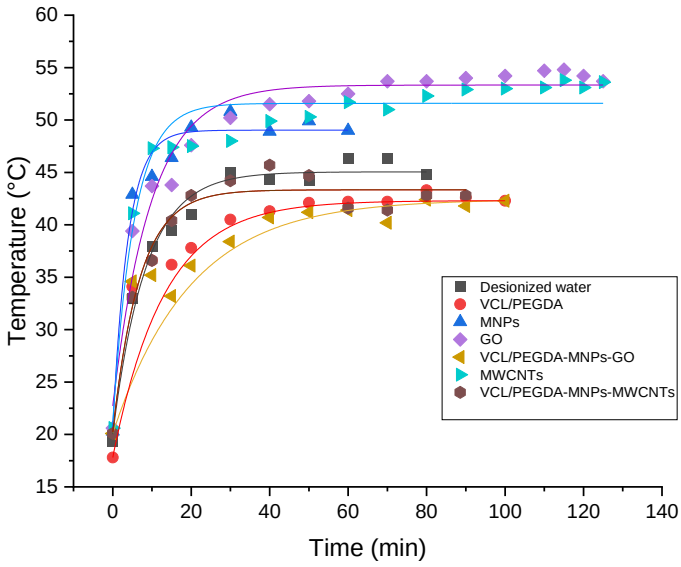

(**a**)

Time (min)	Light dose (J cm^{-2})
0	0
10	39,3
20	78,6
30	117,9
40	157,2
50	196,5
60	235,8
70	275,1
80	314,4
90	353,7
100	393

(**b**)

Figure 8. (**a**) Thermal studies. deionized water (control black line), VCL/PEGDA (red line), MNPs (blue line), GO (violet line), MWCNTs (light blue line), VCL/PEGDA-MNPs-GO (yellow line) and VCL/PEGDA-MNPs-MWCNTs (brown line); (**b**) Light dose. GO = 3.47 μg mL^{-1}, MWCNTs = 3.47 μg mL^{-1}, MNPs= 93.3 μg mL^{-1}.

 doi:10.20944/preprints202201.0037.v1

3.6. *Morphological studies of magnetic nanocomposites*

The functionalized VCL/PEGDA-MNPs-GO-ZnMintPc and VCL/PEGDA-MNPs-MWCNTs-ZnMintPc nanocomposites were characterized by SEM, TEM, EDS and XRD and the results are presented in figures 9, S5, S8, S10, and S12 for GO-based nanocomposites, in figures 10, S6, S9, S11 and S13 for MWCNTs-based nanocomposites and in figure S7 for free-standing MNPs.

The SEM and TEM images in figure 9 show the morphology of (a) carbon nanotubes which have the shape of fibers and in TEM their internal structure and walls, (b) the structure of the GO sheet. In figure 9c we can observe the MNPs, which have a spherical shape with an average size of ~72 nm. Figures 9d and 9e show the morphology of the hydrogel coating MNPs-GO-ZnMintPc and MNPs-MWCNTs-ZnMintPc, so it is difficult to differentiate the structures covered by the hydrogel. In the figure 9f we present the XRD pattern for the MNPs-GO sample, where the diffraction peaks of the Fe nanoparticles decorating the GO are clearly observed at 2θ = 30.27°, 35.6°, 43.3°, 53.7°, 57.1° and 63.0°, indicating that the MNPs retain their original crystalline structure after functionalization [109,110].

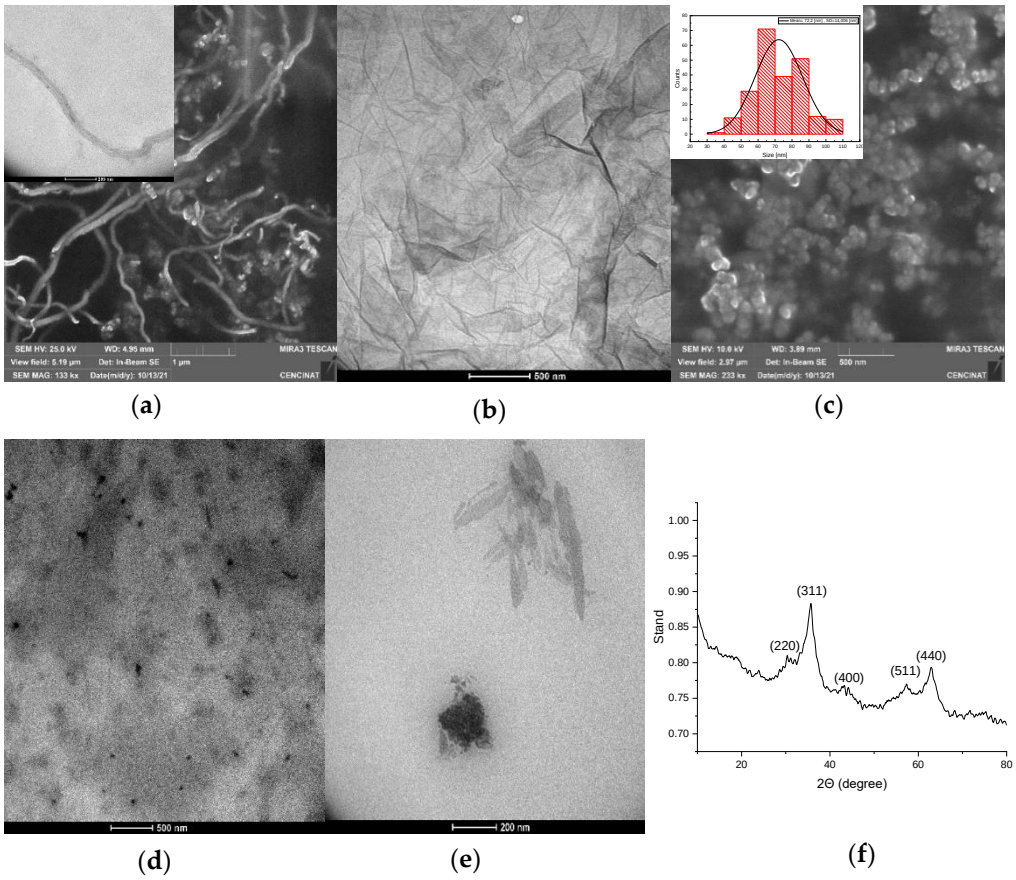

Figure 9. (**a**) SEM and TEM images of purified MWCNTs; (**b**) TEM of GO; (**c**) SEM of MNPs; (**d**) TEM of VCL/PEGDA-MNPs-MWCNTs-ZnMintPc; (**e**) TEM of VCL/PEGDA-MNPs-GO-ZnMintPc; (**f**) XRD analysis of MNPs-GO.

3.7. *Morphological studies of bacterial in magnetic nanocomposites*

To understand the interaction of magnetic nanocomposites with microorganisms, STEM images of *S. aureus, E. coli* bacteria were obtained in the presence of VCL/PEGDA-MNPs-GO-ZnMintPc and VCL/PEGDA-MNPs-MWCNT-ZnMintPc nanocomposites (Figures 10b, 10c, 10e and 10f). In the STEM image of *S. aureus* and *E. coli* (pure, figures 10a and 10d), their structure and morphology are observed without alteration and the

 doi:10.20944/preprints202201.0037.v1

membrane that covers them without ruptures. When interacting with the VCL/PEGDA-MNPs-GO-ZnMintPc and VCL/PEGDA-MNPs-MWCNT-ZnMintPc nanocomposites, no changes were observed in the morphology of the bacteria (images taken 24 hours after the bacterial-nanocomposite solutions were prepared) [111–113]. It was possible to observe how the nanocomposite is capable of completely covering the microorganism, allowing the nanocomposites dispersed in the hydrogel to be photoexcited with the red-light source and obtain the microbial elimination.

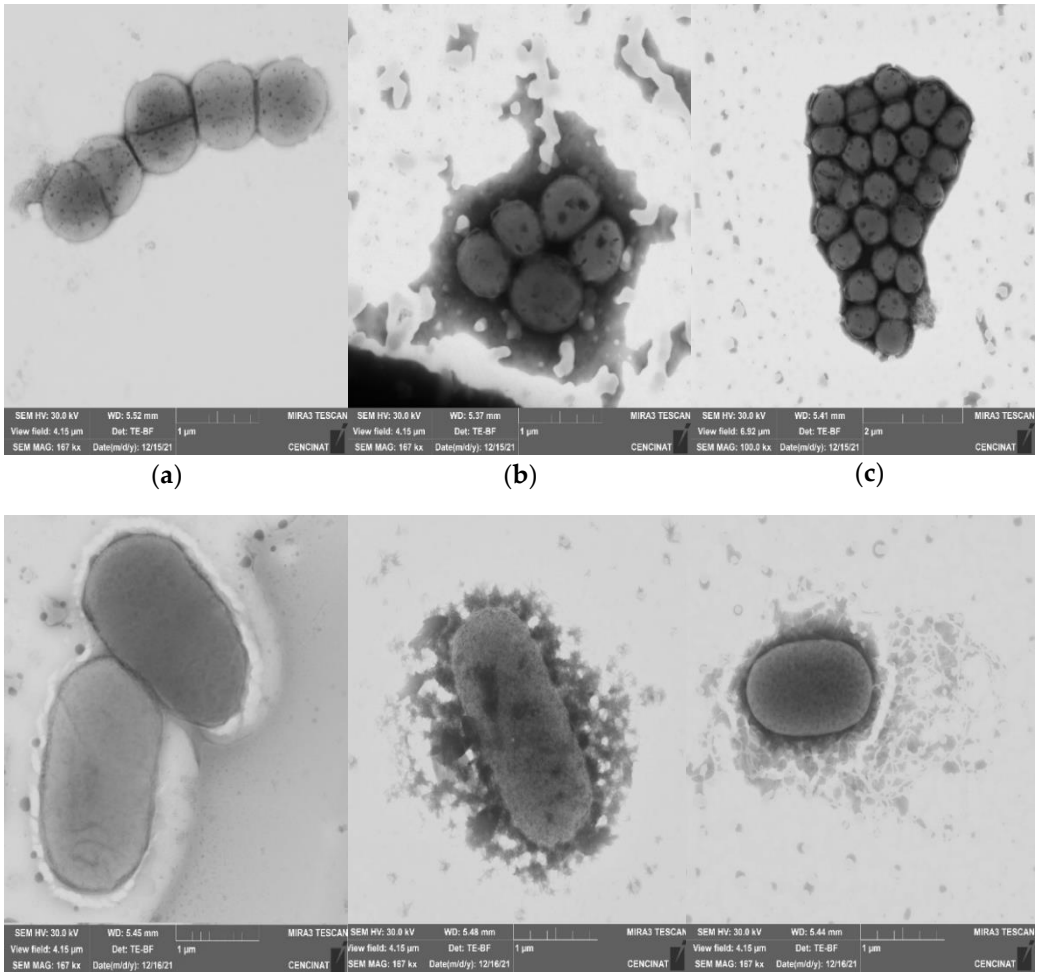

Figure 10: STEM of: (**a**) *S. aureus*; (**b**) *S. aureus*+C1(VCL/PEGDA-MNPs-GO-ZnMintPc); (**c**) *S. aureus*+C2(VCL/PEGDA-MNPs-MWCNTs-ZnMintPc); (**d**) *E. coli;* (**e**) *E. coli*+C1; (**f**) *E. coli*+C2.

3.8. Antimicrobial effect of magnetic nanocomposites

The antimicrobial effect of the VCL/PEGDA-MNPs-GO-ZnMintPc (C1), VCL/PEGDA-MNPs-MWCNTs-ZnMintPc (C2), MNPs-GO (C3) and MNPs-MWCNTs (C4) nanocomposites were evaluated when irradiating with 350 nm red light, 65 mW cm^{-2} in the presence of the microorganisms *S. aureus E. coli* and *C. albicans.*

The results obtained for each colony are present in the histograms of figure 11. The histograms present the evaluation of LOG (CFU mL^{-1}) standardized to 1. Having a concentration of 10^7 CFU mL^{-1} for *S. aureus*, 10^6 CFU mL^{-1} for *E. coli* and 10^5 CFU mL^{-1} for *C. albicans*. Results show that light alone is not capable of eliminating microorganisms (control+light samples) and this can be corroborated in the images obtained from *C. albicans* (figure 12: Control+light sample), that is, to eliminate the microorganism it is necessary to irradiate it in the presence of a nanocomposite (figure 12: C1+light and C2+light).

Preprints (www.preprints.org) | NOT PEER-REVIEWED | Posted: 5 January 2022 doi:10.20944/preprints202201.0037.v1

When irradiating fungi and bacteria with a red LED (630 nm 65 mW cm^{-2}) in the presence of the nanocomposites, it was obtained that the C1 nanocomposite eliminated totality *E. coli, C. albicans* and *S. aureus* partiality. C2 nanocomposite eliminated totality *S. aureus, E. coli* and *C. albicans*. C3 and C4 nanocomposites eliminated the totality of *C. albicans*. Therefore, all nanocomposites can eliminate some of the microorganisms used in this study, with C2 being the best, due to its ability to eliminate the three types of microorganisms [113–115].

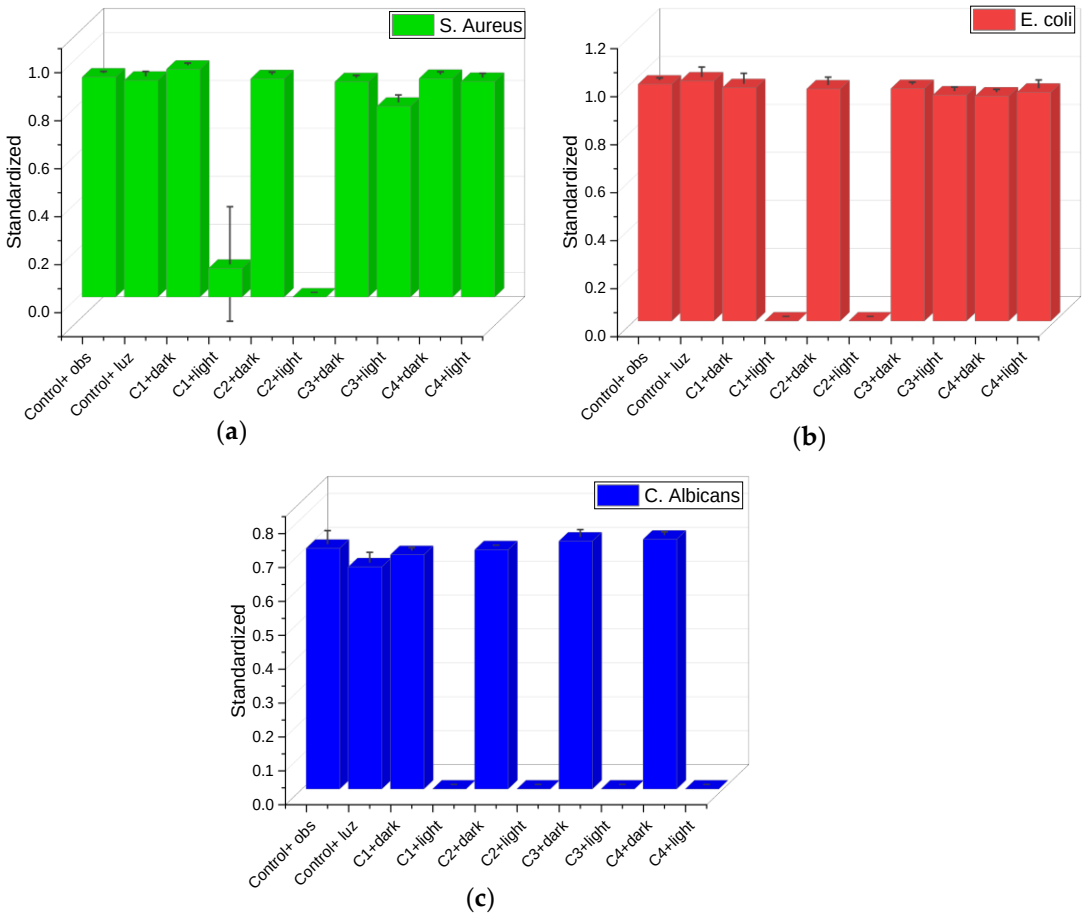

Figure 11. PDT/PTT antimicrobial effect. Standardized result of LOG(UFC/mL) by: (**a**) *S. aureus;* (**b**) *E coli* and (**c**) *C. albicans* based in C1, C2, C3 and C4 nanocomposites. Concentration of MNPs in C1, C2, C3 and C4: 93.3 μg mL^{-1}, Concentration of ZnMintPc in C1 and C2: 8.1 μM, Concentration of GO in C1 and C3: 3.47 μg mL^{-1}, Concentration of MWCNTs in C2 and C4: 3.47 μg mL^{-1}. Time of irradiation: C1 and C2 nanocomposites for 30 min and C3 and C4 for 40 min.

Preprints (www.preprints.org) | NOT PEER-REVIEWED | Posted: 5 January 2022 doi:10.20944/preprints202201.0037.v1

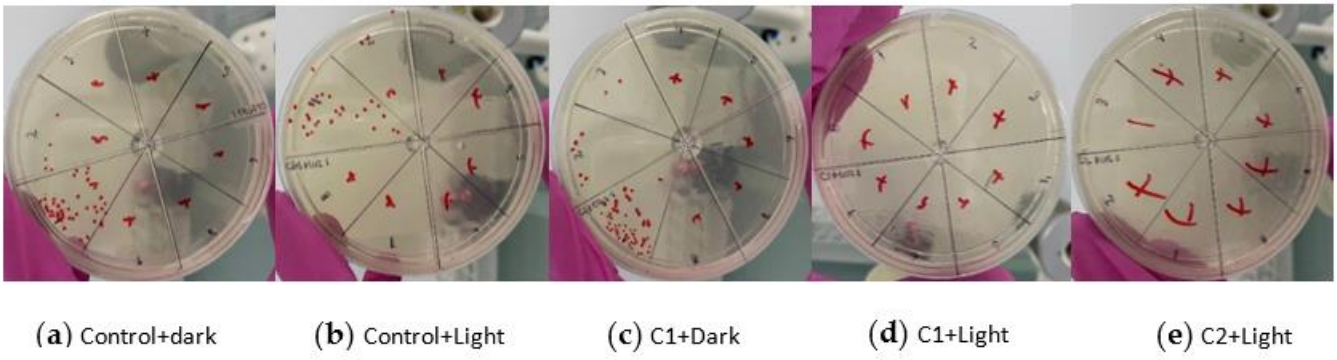

Figure 12. Antimicrobial effect of C1 and C2 nanocomposites in C albicans. C1: GO-MNPs-VGLPEGDA- ZnMintPc, C2: MWCNT-MNPs-VGLPEGDA- ZnMintPc, C3: GO-MNPs-VGLPEGDA, C4: MWCNT-MNPs-VGLPEGDA. Concentration of MNPs in C1, C2, C3 and C4: 93.3 μg mL^{-1}, Concentration of ZnMintPc in C1 and C2: 8.1 μM, Concentration of GO in C1 and C3: 3.47 μg mL^{-1}, Concentration of MWCNTs in C2 and C4: 3.47 μg mL^{-1}.

The samples without hydrogel C3 and C4 only presented a complete response in *C. albicans,* and it could be considered that the photothermic effect allowed microbial elimination, based on the results shown in figure 11c, C3+light and C4+light samples [116]. For the samples with hydrogel and photosensitizer (C1 and C2) it can be concluded that the elimination of the microorganisms *S. aureus, E. coli* and *C. albicans* was produced by the photodynamic effect, based on the results shown in figure 11 C1+light and C2+light samples [114].

According to the results obtained, the VCL/PEGDA-MNPs-GO-ZnMintPc and VCL/PEGDA-MNPs-MWCNTs-ZnMintPc nanocomposites present a ferromagnetic character, typical of nanocomposites with iron nanoparticles and with low saturation magnetization, due to be covered by a diamagnetic hydrogel layer, which agrees with the studies carried out by Donadel et al., 2008; Mahdavi et al., 2013; and; Qu et al., 2010; where they synthesize MNPs for bioapplications and demonstrate that the surface modification causes a reduction in saturation magnetization, presenting values of values between 67 to 22 emu g^{-1} depending on the type of biopolymer to be used [117–119].

Due to the physical and magnetic properties of these nanocomposites, it was shown that they can avoid the early extinction of the fluorescence of PS ZnMintPc, thus improving their photodynamic effect, which is mentioned in the work of Huang et al., 2011 and Xiao et al., 2021. The thermodynamic studies carried out by Kou et al., 2019; Srivastava & Kumar, 2010; and Tager et al., 1993 indicate that VCL and PEGDA have good heat capacities of around 258 and 94 J mol^{-1} K^{-1}, which is why they are usually used to synthesize cryogels, which explains that the nanocomposites covered by the VCL/PEGDA hydrogel are capable of being maintained up to a maximum temperature of 40°C receiving doses of red light of up to 393 J cm^{-2}, which in comparison to nanocomposites without hydrogel, these raise their temperature to around 55 ° C which agrees with the literature [52,102–105].

4. Conclusions

In the present study, the synthesis of magnetic nanocomposites VCL/PEGDA-MNPs-MWCNTs-ZnMintPc and VCL/PEGDA-MNPs-GO-ZnMintPc, was carried out: in order to eliminate three types of microbial colonies: *S. aureus, E. coli* and *C. albicans.*

After the synthesis the synthesis of these nanocomposites was carried out their optical, magnetic and morphological characterizations showed that, nanocomposites based on GO and MWCNTS decorated with iron MNPS and ZnMintPc PS, anchored to these structures and covered by the VCL/PEGDA hydrogel.

The optical properties of these nanocomposites give them the ability to prevent the rapid disintegration of PS, which is important in PDT.

In the photodynamic analyzes was studied the nanocomposites VCL/PEGDA-MNPs-MWCNTs-ZnMintPc and VCL/PEGDA-MNPs-GO-ZnMintPc for their applicability in PDT with low dose red light, and it was observed that the nanocomposite containing GO and PS ZnMintPc has a higher efficiency, since it produces a faster photobleaching of DPBF, because it is capable of transporting a greater amount of ZnMintPc and MNPs, due to its large specific area, in addition GO contributes to PS in the formation of $^1O_2$. Also, since the nanocomposites are coated with a hydrogel, they are suitable for controlled PS release system which tend to indicate promising applications for PDT.

the nanocomposite that contains GO and PS ZnMintPc has a higher efficiency, since it produces a faster photobleaching of DPBF, which is due to the fact that it is capable of transporting a greater amount of ZnMintPc and MNPs, due to its large specific area, in addition the GO contributes to PS in the formation of 1O2.

Finally, we demonstrated that the VCL/PEGDA-MNPs-GO-ZnMintPc nanocomposite was able to eliminate colonies of *E. coli* and *C. albicans* and the VCL/PEGDA-MNPs-MWCNTs-ZnMintPc nanocomposite eliminated the three types of microorganism, therefore which can be considered as a broad-spectrum antimicrobial agent in PDT and PTT

Supplementary Materials: YES

Author Contributions:

Coralia Cuadrado: Manuscript writing, synthesis of magnetic nanocomposites, physico-chemical studies.

Antonio Díaz: Synthesis of the VGLPEG-DA hydrogel, revision of the manuscript.

Kleber Campana: Characterization of magnetic nanocomposites using Raman and FT-IR spectroscopy

Eric Cardona Romani: synthesis of Oxidized Graphene and review of the manuscript

Francisco Quiroz: Helps in the synthesis of magnetic nanocomposites.

Stefania Nardecchia: synthesis of Oxidized Graphene and review of the manuscript

Alexis Debut: Characterization of magnetic nanocomposites using TEM, SEM, STEM and DRX. Review of the manuscript.

Karla Vizuete: Characterization of magnetic nanocomposites using TEM, SEM, STEM and DRX

Dario Niebieskikwiat: DN performed the magnetic measurements and data analysis, and also contributed with the writing of the manuscript.

Camilo Ernesto Ávila: Studies of the antimicrobial effect of magnetic nanocomposites.

Mateo Alejandro Salazar: Studies of the antimicrobial effect of magnetic nanocomposites.

Cristina Cecibel Garzón-Romero: Studies of the antimicrobial effect of magnetic nanocomposites. Review of the manuscript related to the antimicrobial effect.

Ailín Amira Blasco: Studies of the antimicrobial effect of magnetic nanocomposites.

Miryan Rosita Rivera: Studies of the antimicrobial effect of magnetic nanocomposites. Contribution with materials and equipment for the defect study.

María Paulina Romero: Design of the experiments, revision of the manuscript, direction of the antimicrobial studies.

Funding: National Polytechnic School through the PIIF-20-05 project. Research Office of the Pontificia Universidad Católica del Ecuador project code QINV0324 - IINV529010100.

Acknowledgments: The Zinc Menthol-Phthalocyanine was given by the Federal University of São Carlos-Brazil. To student Carlos Moscoso for helping on experiments in micro-organisms. To the

National Polytechnic School through the PIIF-20-05 project. To the Research Office of the Pontificia Universidad Católica del Ecuador project code QINV0324 - IINV529010100

Conflicts of Interest: The authors declare no conflict of interest.

References

1. Organization, W.H. *Managing Epidemics: Key Facts About Major Deadly Diseases*; 2018; Vol. 1; ISBN 9789241565530.
2. World Health Organization Antimicrobial resistance Available online: https://www.who.int/news-room/fact-sheets/detail/antimicrobial-resistance (accessed on Dec 19, 2021).
3. Ali, A.; Ovais, M.; Cui, X.; Rui, Y.K.; Chen, C. Safety Assessment of Nanomaterials for Antimicrobial Applications. *Chem. Res. Toxicol.* **2020**, *33*, 1082–1109, doi:10.1021/ACS.CHEMRESTOX.9B00519.
4. Akhavan, O.; Ghaderi, E. Toxicity of Graphene and Graphene Oxide Nanowalls Against Bacteria. *ACS Nano* **2010**, *4*, 5731–5736, doi:10.1021/NN101390X.
5. Gunawan, C.; Teoh, W.Y.; Marquis, C.P.; Amal, R. Cytotoxic origin of copper(II) oxide nanoparticles: Comparative studies with micron-sized particles, leachate, and metal salts. *ACS Nano* **2011**, *5*, 7214–7225, doi:10.1021/NN2020248/SUPPL_FILE/NN2020248_SI_001.PDF.
6. Zou, X.; Zhang, L.; Wang, Z.; Luo, Y. Mechanisms of the Antimicrobial Activities of Graphene Materials. *J. Am. Chem. Soc.* **2016**, *138*, 2064–2077, doi:10.1021/jacs.5b11411.
7. Al-Jumaili, A.; Alancherry, S.; Bazaka, K.; Jacob, M. V. Review on the Antimicrobial Properties of Carbon Nanostructures. *Mater. 2017, Vol. 10, Page 1066* **2017**, *10*, 1066, doi:10.3390/MA10091066.
8. Karahan, H.E.; Wiraja, C.; Xu, C.; Wei, J.; Wang, Y.; Wang, L.; Liu, F.; Chen, Y. Graphene Materials in Antimicrobial Nanomedicine: Current Status and Future Perspectives. *Adv. Healthc. Mater.* **2018**, *7*, 1701406, doi:10.1002/ADHM.201701406.
9. Romero, M.P.; Marangoni, V.S.; de Faria, C.G.; Leite, I.S.; Silva, C. de C.C. e.; Maroneze, C.M.; Pereira-da-Silva, M.A.; Bagnato, V.S.; Inada, N.M. Graphene Oxide Mediated Broad-Spectrum Antibacterial Based on Bimodal Action of Photodynamic and Photothermal Effects. *Front. Microbiol.* **2020**, *10*, 2995, doi:10.3389/fmicb.2019.02995.
10. Peng, R.; Luo, Y.; Cui, Q.; Wang, J.; Li, L. Near-Infrared Conjugated Oligomer for Effective Killing of Bacterial through Combination of Photodynamic and Photothermal Treatment. *ACS Appl. Bio Mater.* **2020**, *3*, 1305–1311, doi:10.1021/ACSABM.9B01242/SUPPL_FILE/MT9B01242_SI_001.PDF.
11. Xu, J.W.; Yao, K.; Xu, Z.K. Nanomaterials with a photothermal effect for antibacterial activities: an overview. *Nanoscale* **2019**, *11*, 8680–8691, doi:10.1039/C9NR01833F.
12. Dąbrowski, J.M. Reactive Oxygen Species in Photodynamic Therapy: Mechanisms of Their Generation and Potentiation. In *Advances in Inorganic Chemistry*; Academic Press Inc., 2017; Vol. 70, pp. 343–394.
13. Henderson, B.; Dougherty, T. How does photodynamic therapy work? *Photochem.* **1992**.
14. Kwiatkowski, S.; Knap, B.; Przystupski, D.; Saczko, J.; Kędzierska, E.; Knap-Czop, K.; Kotlińska, J.; Michel, O.; Kotowski, K.; Kulbacka, J. Photodynamic therapy – mechanisms, photosensitizers and combinations. *Biomed. Pharmacother.* 2018, *106*, 1098–1107.
15. Chen, J.; Fan, T.; Xie, Z.; Zeng, Q.; Xue, P.; Zheng, T.; Chen, Y.; Luo, X.; Zhang, H. Advances in nanomaterials for photodynamic therapy applications: Status and challenges. *Biomaterials* 2020, *237*, 119827.
16. Banerjee, S.M.; MacRobert, A.J.; Mosse, C.A.; Periera, B.; Bown, S.G.; Keshtgar, M.R.S. Photodynamic therapy: Inception to application in breast cancer. *Breast* 2017, *31*, 105–113.
17. Wu, D.; Fan, Y.; Yan, H.; Li, D.; Zhao, Z.; Chen, X.; Yang, X.; Liu, X. Oxidation-sensitive polymeric nanocarrier-mediated cascade PDT chemotherapy for synergistic cancer therapy and potentiated checkpoint blockade immunotherapy. *Chem. Eng. J.* **2020**, *404*, doi:10.1016/j.cej.2020.126481.

18. Railkar, R.; Agarwal, P.K. Photodynamic Therapy in the Treatment of Bladder Cancer: Past Challenges and Current Innovations. *Eur. Urol. Focus* 2018, *4*, 509–511.
19. Allison, R.R.; Downie, G.H.; Cuenca, R.; Hu, X.-H.; Childs, C.J.; Sibata, C.H. Photosensitizers in clinical PDT. *Photodiagnosis Photodyn. Ther.* **2004**, *1*, 27–42, doi:10.1016/S1572-1000(04)00007-9.
20. Wharton, T.; Gali, H.; Hamblin, M. Photosensitizers for Targeted Photodynamic Therapy. **2009**, *8*, 1–23.
21. Bonnett, R.; Diamond, I.; Granelli, S.; McDonagh, A.F.; Nielsen, S.; Wilson, C.B.; Jaenicke, R.; Böhm, F.; Marston, G.; Truscott, T.G.; et al. Photosensitizers of the porphyrin and phthalocyanine series for photodynamic therapy. *Chem. Soc. Rev.* **1995**, *24*, 19, doi:10.1039/cs9952400019.
22. Romero, M.P. Estudo da Interação de Fotossensibilizantes Derivados de Ftalocianinas com Sistemas de Distribuição de Fármacos para Terapia Fotodinâmica, Pontifícia Universidade Católica do Rio de Janeiro: Rio de Janeiro, Brazil, 2012.
23. Zhou, L.; Liu, J.H.; Zhang, J.; Wei, S.H.; Feng, Y.Y.; Zhou, J.H.; Yu, B.Y.; Shen, J. A new sol-gel silica nanovehicle preparation for photodynamic therapy in vitro. *Int. J. Pharm.* **2010**, *386*, 131–137, doi:10.1016/j.ijpharm.2009.11.010.
24. Chowdhary, R.; Dolphin, D.; Donnelly, R.; McCarron, P.; Chowdhary, R.; Dolphin, D. Drug delivery systems for photodynamic therapy.
25. Calixto, G.; Bernegossi, J.; de Freitas, L.; Fontana, C.; Chorilli, M. Nanotechnology-Based Drug Delivery Systems for Photodynamic Therapy of Cancer: A Review. *Molecules* **2016**, *21*, 342, doi:10.3390/molecules21030342.
26. Nombona, N.; Antunes, E.; Chidawanyika, W.; Kleyi, P.; Tshentu, Z.; Nyokong, T. Synthesis, photophysics and photochemistry of phthalocyanine-ε-polylysine conjugates in the presence of metal nanoparticles against Staphylococcus aureus. *J. Photochem. Photobiol. A Chem.* **2012**, *233*, 24–33, doi:10.1016/j.jphotochem.2012.02.012.
27. Li, Y.; Dong, H.; Li, Y.; Shi, D. Graphene-based nanovehicles for photodynamic medical therapy. *Int. J. Nanomedicine* 2015, *10*, 2451–2459.
28. Chatterjee, D.K.; Fong, L.S.; Zhang, Y. Nanoparticles in photodynamic therapy: An emerging paradigm. *Adv. Drug Deliv. Rev.* 2008, *60*, 1627–1637.
29. Sanginario, A.; Miccoli, B.; Demarchi, D. Carbon Nanotubes as an Effective Opportunity for Cancer Diagnosis and Treatment. *Biosensors* 2017, *7*, 9.
30. Guo, Q.; Shen, X. tao; Li, Y. yuan; Xu, S. qing Carbon nanotubes-based drug delivery to cancer and brain. *J. Huazhong Univ. Sci. Technol. - Med. Sci.* **2017**, *37*, 635–641, doi:10.1007/s11596-017-1783-z.
31. Sundaram, P.; Abrahamse, H. Effective Photodynamic Therapy for Colon Cancer Cells Using Chlorin e6 Coated Hyaluronic Acid-Based Carbon Nanotubes. *Int. J. Mol. Sci.* **2020**, *21*, 4745, doi:10.3390/ijms21134745.
32. Augustine, S.; Singh, J.; Srivastava, M.; Sharma, M.; Das, A.; Malhotra, B.D. Recent advances in carbon based nanosystems for cancer theranostics. *Biomater. Sci.* 2017, *5*, 901–952.
33. Jovanović, S.; Marković, Z.; Marković, B.T. Carbon-based nanomaterials as agents for photodynamic therapy. *Int. J. Cancer Res. Prev.* **2017**, *10*, 125–172.
34. Lee, J.; Kim, J.; Kim, S.; Min, D.H. Biosensors based on graphene oxide and its biomedical application. *Adv. Drug Deliv. Rev.* 2016, *105*, 275–287.
35. Chauhan, N.; Maekawa, T.; Kumar, D.N.S. Graphene based biosensors - Accelerating medical diagnostics to new-dimensions. *J. Mater. Res.* 2017, *32*, 2860–2882.
36. Farrera, C.; Torres Andón, F.; Feliu, N. Carbon Nanotubes as Optical Sensors in Biomedicine. *ACS Nano* 2017, *11*, 10637–10643.
37. Yapici, M.; Alkhidir, T. Intelligent Medical Garments with Graphene-Functionalized Smart-Cloth ECG Sensors. *Sensors* **2017**, *17*, 875, doi:10.3390/s17040875.
38. Iijima, S. Helical microtubules of graphitic carbon. *Nature* **1991**, *354*, 56–58, doi:10.1038/354056a0.

39. Cheung, W.; Pontoriero, F.; Taratula, O.; Chen, A.M.; He, H. DNA and carbon nanotubes as medicine. *Adv. Drug Deliv. Rev.* **2010**, *62*, 633–649, doi:10.1016/j.addr.2010.03.007.
40. Reilly, R.M. Carbon nanotubes: potential benefits and risks of nanotechnology in nuclear medicine. *J. Nucl. Med.* **2007**, *48*, 1039–42, doi:10.2967/jnumed.107.041723.
41. Menezes, B.R.C. De; Rodrigues, K.F.; Fonseca, B.C.D.S.; Ribas, R.G.; Montanheiro, T.L.D.A.; Thim, G.P. Recent advances in the use of carbon nanotubes as smart biomaterials. *J. Mater. Chem. B* 2019, *7*, 1343–1360.
42. Herlem, G.; Picaud, F.; Girardet, C.; Micheau, O. *Carbon Nanotubes: Synthesis, Characterization, and Applications in Drug-Delivery Systems*; Elsevier Inc., 2019; ISBN 9780128140338.
43. Muthoosamy, K.; G. Bai, R.; Manickam, S. Graphene and Graphene Oxide as a Docking Station for Modern Drug Delivery System.
44. Wei, Y.; Zhou, F.; Zhang, D.; Chen, Q.; Xing, D. A graphene oxide based smart drug delivery system for tumor mitochondria-targeting photodynamic therapy. *Nanoscale* **2016**, *8*, 3530–3538, doi:10.1039/c5nr07785k.
45. Sajjadi, M.; Nasrollahzadeh, M.; Jaleh, B.; Jamalipour Soufi, G.; Iravani, S. Carbon-based nanomaterials for targeted cancer nanotherapy: recent trends and future prospects. *J. Drug Target.* **2021**, 1–78, doi:10.1080/1061186x.2021.1886301.
46. Maleki, R.; Afrouzi, H.H.; Hosseini, M.; Toghraie, D.; Rostami, S. Molecular dynamics simulation of Doxorubicin loading with N-isopropyl acrylamide carbon nanotube in a drug delivery system. *Comput. Methods Programs Biomed.* **2020**, *184*, 105303, doi:10.1016/j.cmpb.2019.105303.
47. Qin, X.; Li, Y. Strategies To Design and Synthesize Polymer-Based Stimuli-Responsive Drug-Delivery Nanosystems. *ChemBioChem* **2020**, *21*, 1236–1253, doi:10.1002/cbic.201900550.
48. Geim, A.K.; Novoselov, K.S. The rise of graphene. *Nat. Mater.* **2007**, *6*, 183–91, doi:10.1038/nmat1849.
49. Avouris, P.; Xia, F. Graphene applications in electronics and photonics. *MRS Bull.* **2012**, *37*, 1225–1234, doi:10.1557/mrs.2012.206.
50. Perreault, F.; Fonseca de Faria, A.; Elimelech, M. Environmental applications of graphene-based nanomaterials. *Chem. Soc. Rev.* **2015**, *44*, 5861–5896, doi:10.1039/C5CS00021A.
51. Singh, D.P.; Herrera, C.E.; Singh, B.; Singh, S.; Singh, R.K.; Kumar, R. Graphene oxide: An efficient material and recent approach for biotechnological and biomedical applications. *Mater. Sci. Eng. C* 2018, *86*, 173–197.
52. Estelrich, J.; Busquets, M.A. Iron Oxide Nanoparticles in Photothermal Therapy. *Mol. 2018, Vol. 23, Page 1567* **2018**, *23*, 1567, doi:10.3390/MOLECULES23071567.
53. Tapeinos, C. Magnetic Nanoparticles and Their Bioapplications. In *Smart Nanoparticles for Biomedicine*; Elsevier, 2018; pp. 131–142 ISBN 9780128141571.
54. Cardoso, V.F.; Francesko, A.; Ribeiro, C.; Bañobre-López, M.; Martins, P.; Lanceros-Mendez, S. Advances in Magnetic Nanoparticles for Biomedical Applications. *Adv. Healthc. Mater.* 2018, *7*, 1700845.
55. Li, X.; Wei, J.; Aifantis, K.E.; Fan, Y.; Feng, Q.; Cui, F.Z.; Watari, F. Current investigations into magnetic nanoparticles for biomedical applications. *J. Biomed. Mater. Res. - Part A* 2016, *104*, 1285–1296.
56. Miri, A.; Khatami, M.; Sarani, M. Biosynthesis, Magnetic and Cytotoxic Studies of Hematite Nanoparticles. *J. Inorg. Organomet. Polym. Mater.* **2020**, *30*, 767–774, doi:10.1007/s10904-019-01245-6.
57. Rajendran, K.; Sen, S.; Suja, G.; Senthil, S.L.; Kumar, T.V. Evaluation of cytotoxicity of hematite nanoparticles in bacteria and human cell lines. *Colloids Surfaces B Biointerfaces* **2017**, *157*, 101–109, doi:10.1016/j.colsurfb.2017.05.052.
58. Yu, Q.; Xiong, X. qin; Zhao, L.; Xu, T. ting; Bi, H.; Fu, R.; Wang, Q. hua Biodistribution and Toxicity Assessment of Superparamagnetic Iron Oxide Nanoparticles In Vitro and In Vivo. *Curr. Med. Sci.* **2018**, *38*, 1096–1102, doi:10.1007/s11596-018-1989-8.
59. Avval, Z.M.; Malekpour, L.; Raeisi, F.; Babapoor, A.; Mousavi, S.M.; Hashemi, S.A.; Salari, M. Introduction of magnetic and

supermagnetic nanoparticles in new approach of targeting drug delivery and cancer therapy application. *Drug Metab. Rev.* 2020, *52*, 157–184.

60. Ramasamy, M.; Kumar, P.S.; Varadan, V.K. Magnetic nanotubes for drug delivery. In Proceedings of the Nanosensors, Biosensors, Info-Tech Sensors and 3D Systems 2017; SPIE, 2017; Vol. 10167, p. 1016715.
61. Forcada, J.; Imaz, A.; San Martín, A.; Ramos, J.; Van, Alex, M.; Heuts, Johannes A., P. Cationic nanogels for biotechnological uses. *U.S. Pat. Appl. No. 13/635* **2011**, 759.
62. Ramos, J.; Imaz, A.; Forcada, J.; Oh, J.K.; Drumright, R.; Siegwart, D.J.; Matyjaszewski, K.; Lyon, L.A.; Meng, Z.; Singh, N.; et al. Temperature-sensitive nanogels: poly(N-vinylcaprolactam) versus poly(N-isopropylacrylamide). *Polym. Chem.* **2012**, *3*, 852–856, doi:10.1039/C2PY00485B.
63. Romero, J.F.; Diaz-Barrios, A.; Gonzalez, G. Biocompatible thermo-responsive N-vinylcaprolactam based hydrogels for controlled drug delivery systems. *Rev. Bionatura* **2021**, *6*, 1712–1719, doi:10.21931/RB/2021.06.02.8.
64. Hummers, W.S.; Offeman, R.E. Preparation of Graphitic Oxide. *J. Am. Chem. Soc.* **1958**, *80*, 1339, doi:10.1021/ja01539a017.
65. Zhang, X.; Luminescence, X.L.-J. of; 2011, undefined The photostability and fluorescence properties of diphenylisobenzofuran. *Elsevier* **2011**, doi:10.1016/j.jlumin.2011.05.048.
66. Cunha, C.; Panseri, S.; Iannazzo, D.; Piperno, A.; Pistone, A.; Fazio, M.; Russo, A.; Marcacci, M.; Galvagno, S. Hybrid composites made of multiwalled carbon nanotubes functionalized with Fe 3 O 4 nanoparticles for tissue engineering applications. *Nanotechnology* **2012**, *23*, 465102, doi:10.1088/0957-4484/23/46/465102.
67. Navamani, J. Development of Nanoprobe for the Determination of Blood Cholesterol. *J. Biosens. Bioelectron.* **2012**, *03*, 15, doi:10.4172/2155-6210.1000122.
68. Pourzamani, H.; Hajizadeh, Y.; Fadaei, S. Efficiency enhancement of multi-walled carbon nanotubes by ozone for benzene removal from aqueous solution. *Int. J. Environ. Health Eng.* **2015**, *4*, 29, doi:10.4103/2277-9183.163972.
69. Li, J.; Huang, Y.; Ding, Y.; Yang, Z.; Li, S.; Zhou, X. Shell-isolated nanoparticle-enhanced Raman spectroscopy. *Nature* **2010**.
70. Al-Ruqeishi, M.S.; Mohiuddin, T.; Al-Moqbali, M.; Al-Shukaili, H.; Al-Mamari, S.; Al-Rashdi, H.; Al-Busaidi, R.; Sreepal, V.; Nair, R.R. Graphene Oxide Synthesis: Optimizing the Hummers and Marcano Methods. *Nanosci. Nanotechnol. Lett.* **2020**, *12*, 88–95, doi:10.1166/nnl.2020.3074.
71. Abrinaei, F.; Kimiagar, S.; Zolghadr, S. Hydrothermal synthesis of hematite-GO nanocomposites at different GO contents and potential application in nonlinear optics. *Opt. Mater. (Amst).* **2019**, *96*, 109285, doi:10.1016/j.optmat.2019.109285.
72. Santoro, G.; Domingo, C. Espectroscopía Raman de nanotubos de carbono. **2007**.
73. Dresselhaus, M.; Dresselhaus, G.; Saito, R.; Jorio, A. Raman spectroscopy of carbon nanotubes. *Phys. Rep.* **2005**.
74. Marković, Z.; Jovanović, S.; Kleut, D.; Romčević, N.; Jokanović, V.; Trajković, V.; Todorović-Marković, B. Comparative study on modification of single wall carbon nanotubes by sodium dodecylbenzene sulfonate and melamine sulfonate superplasticiser. *Appl. Surf. Sci.* **2009**, *255*, 6359–6366, doi:10.1016/j.apsusc.2009.02.016.
75. L. Bokobza, J.Z. Raman spectroscopic characterization of multiwall carbon nanotubes and of composites. *eXPRESS Polym. Lett.* **2012**, *6*, 601–608, doi:10.3144/expresspolymlett.2012.63.
76. Krysa, J.; Zlamal, M.; Kment, S.; Brunclikova, M.; Hubicka, Z. TiO2 and Fe2O3 Films for Photoelectrochemical Water Splitting. *Molecules* **2015**, *20*, 1046–1058, doi:10.3390/molecules20011046.
77. Krolop, P.; Jantschke, A.; Gilbricht, S.; Niiranen, K.; Seifert, T. Mineralogical Imaging for Characterization of the Per Geijer Apatite Iron Ores in the Kiruna District, Northern Sweden: A Comparative Study of Mineral Liberation Analysis and Raman Imaging. *Minerals* **2019**, *9*, 544, doi:10.3390/min9090544.
78. Jung, J.-Y.; Kim, S.-H.; Kang, E.-T.; Kim, J.-H.; Han, K.-S.; Hwang, K.-T.; Cho, W.-S. Synthesis of Ga 2 O 3 powders by precipitation method. *J. Korean Cryst. Growth Cryst. Technol.* **2014**, *24*, 8–14, doi:10.6111/jkcgct.2014.24.1.008.
79. Cançado, L.G.; Jorio, A.; Ferreira, E.H.M.; Stavale, F.; Achete, C.A.; Capaz, R.B.; Moutinho, M.V.O.; Lombardo, A.; Kulmala,

T.S.; Ferrari, A.C. Quantifying defects in graphene via Raman spectroscopy at different excitation energies. *Nano Lett.* **2011**, *11*, 3190–3196, doi:10.1021/nl201432g.

80. Muhammad Hafiz, S.; Ritikos, R.; Whitcher, T.J.; Md. Razib, N.; Bien, D.C.S.; Chanlek, N.; Nakajima, H.; Saisopa, T.; Songsiriritthigul, P.; Huang, N.M.; et al. A practical carbon dioxide gas sensor using room-temperature hydrogen plasma reduced graphene oxide. *Sensors Actuators, B Chem.* **2014**, *193*, 692–700, doi:10.1016/j.snb.2013.12.017.
81. Ramirez, S.; Chan, K.; Hernandez, R.; Recinos, E.; Hernandez, E.; Salgado, R.; Khitun, A.G.; Garay, J.E.; Balandin, A.A. Thermal and magnetic properties of nanostructured densified ferrimagnetic composites with graphene - graphite fillers. *JMADE* **2017**, *118*, 75–80, doi:10.1016/j.matdes.2017.01.018.
82. Satheesh, M.; Paloly, A.R.; Krishna Sagar, C.K.; Suresh, K.G.; Bushiri, M.J. Improved Coercivity of Solvothermally Grown Hematite (α-Fe2O3) and Hematite/Graphene Oxide Nanocomposites (α-Fe2O3/GO) at Low Temperature. *Phys. Status Solidi Appl. Mater. Sci.* **2018**, *215*, 1700705, doi:10.1002/pssa.201700705.
83. Sajitha, E.P.; Prasad, V.; Subramanyam, S. V.; Mishra, A.K.; Sarkar, S.; Bansal, C. Size-dependent magnetic properties of iron carbide nanoparticles embedded in a carbonmatrix. *J. Phys. Condens. Matter* **2007**, *19*, 046214, doi:10.1088/0953-8984/19/4/046214.
84. Lipert, K.; Kazmierezak, J.; Pelech, I.; Narkiewicz, U.; Slawska-Waniewska, A.; Lachowicz, H.K. Magnetic properties of cementite (Fe~ 3C) nanoparticle agglomerates in a carbon matrix. *Mater. Sci.* **2007**, *25*, 399.
85. Grössinger, R. Correlation between the inhomogeneity and the magnetic anisotropy in polycrystalline ferromagnetic materials. *J. Magn. Magn. Mater.* **1982**, *28*, 137–142, doi:10.1016/0304-8853(82)90037-3.
86. Hauser, H.; Jiles, D.C.; Melikhov, Y.; Li, L.; Grössinger, R. An approach to modeling the dependence of magnetization on magnetic field in the high field regime. *J. Magn. Magn. Mater.* **2006**, *300*, 273–283, doi:10.1016/J.JMMM.2005.05.017.
87. Batlle, X.; García Del Muro, M.; Tejada, J.; Pfeiffer, H.; Görnert, P.; Sinn, E. Magnetic study of M-type doped barium ferrite nanocrystalline powders. *J. Appl. Phys.* **1993**, *74*, 3333–3340, doi:10.1063/1.354558.
88. Kodama, R.H. Magnetic nanoparticles. *J. Magn. Magn. Mater.* **1999**, *200*, 359–372, doi:10.1016/S0304-8853(99)00347-9.
89. Zhang, D.; Klabunde, K.; Sorensen, C.; Hadjipanayis, G. Magnetization temperature dependence in iron nanoparticles. *Phys. Rev. B - Condens. Matter Mater. Phys.* **1998**, *58*, 14167–14170, doi:10.1103/PHYSREVB.58.14167.
90. Xiao, G.; Chien, C.L. Temperature dependence of spontaneous magnetization of ultrafine Fe particles in Fe-SiO2 granular solids. *J. Appl. Phys.* **1987**, *61*, 3308–3310, doi:10.1063/1.338891.
91. Romero, M.P.; Gobo, N.R.S.; de Oliveira, K.T.; Iamamoto, Y.; Serra, O.A.; Louro, S.R.W. Photophysical properties and photodynamic activity of a novel menthol–zinc phthalocyanine conjugate incorporated in micelles. *J. Photochem. Photobiol. A Chem.* **2013**, *253*, 22–29, doi:10.1016/j.jphotochem.2012.12.009.
92. Nunes, S.M.T.M.T.; Sguilla, F.S.S.; Tedesco, A.C.C. Photophysical studies of zinc phthalocyanine and chloroaluminum phthalocyanine incorporated into liposomes in the presence of additives. *Brazilian J. Med. Biol. Res.* **2004**, *37*, 273–284, doi:10.1590/S0100-879X2004000200016.
93. Wang, Y.H.; Song, X.; Shao, S.; Zhong, H.; Lin, F. An efficient, soluble, and recyclable multiwalled carbon nanotubes-supported TEMPO for oxidation of alcohols. *RSC Adv.* **2012**, *2*, 7693, doi:10.1039/c2ra21206d.
94. Saxena, S.; Tyson, T.A.; Shukla, S.; Negusse, E.; Chen, H.; Bai, J. Investigation of structural and electronic properties of graphene oxide. *Appl. Phys. Lett.* **2011**, *99*, 013104, doi:10.1063/1.3607305.
95. Rose, A.; Raghavan, N.; Thangavel, S.; Uma Maheswari, B.; Nair, D.P.; Venugopal, G. Investigation of cyclic voltammetry of graphene oxide/polyaniline/polyvinylidene fluoride nanofibers prepared via electrospinning. *Mater. Sci. Semicond. Process.* **2015**, *31*, 281–286, doi:10.1016/j.mssp.2014.10.051.
96. Çiplak, Z.; Yildiz, N.; Çalimli, A. Investigation of Graphene/Ag Nanocomposites Synthesis Parameters for Two Different Synthesis Methods. *Fullerenes, Nanotub. Carbon Nanostructures* **2015**, *23*, 361–370, doi:10.1080/1536383X.2014.894025.

97. Chen, P.; Marshall, A.S.; Chi, S.H.; Yin, X.; Perry, J.W.; J????kle, F. Luminescent Quadrupolar Borazine Oligomers: Synthesis, Photophysics, and Two-Photon Absorption Properties. *Chem. - A Eur. J.* **2015**, *21*, 18237–18247, doi:10.1002/chem.201502268.
98. Meier, H.; Gerold, J.; Kolshorn, H.; M??hling, B. Extension of Conjugation Leading to Bathochromic or Hypsochromic Effects in OPV Series. *Chem. - A Eur. J.* **2004**, *10*, 360–370, doi:10.1002/chem.200305447.
99. Wu, W.; Shen, J.; Gai, Z.; Hong, K.; Banerjee, P.; Zhou, S. Multi-functional core-shell hybrid nanogels for pH-dependent magnetic manipulation, fluorescent pH-sensing, and drug delivery. *Biomaterials* **2011**, *32*, 9876–9887, doi:10.1016/j.biomaterials.2011.08.082.
100. Wu, W.; Shen, J.; Banerjee, P.; Zhou, S. Core-shell hybrid nanogels for integration of optical temperature-sensing, targeted tumor cell imaging, and combined chemo-photothermal treatment. *Biomaterials* **2010**, *31*, 7555–7566, doi:10.1016/j.biomaterials.2010.06.030.
101. Sánchez-Iglesias, A.; Grzelczak, M.; Rodríguez-González, B.; Guardia-Girós, P.; Pastoriza-Santos, I.; Pérez-Juste, J.; Prato, M.; Liz-Marzán, L.M. Synthesis of multifunctional composite microgels via in situ Ni growth on pNIPAM-coated au nanoparticles. *ACS Nano* **2009**, *3*, 3184–3190, doi:10.1021/nn9006169.
102. Dong, X.; Sun, Z.; Wang, X.; Leng, X. An innovative MWCNTs/DOX/TC nanosystem for chemo-photothermal combination therapy of cancer. *Nanomedicine Nanotechnology, Biol. Med.* **2017**, *13*, 2271–2280, doi:10.1016/J.NANO.2017.07.002.
103. Burke, A.R.; Singh, R.N.; Carroll, D.L.; Wood, J.C.S.; D'Agostino, R.B.; Ajayan, P.M.; Torti, F.M.; Torti, S. V. The resistance of breast cancer stem cells to conventional hyperthermia and their sensitivity to nanoparticle-mediated photothermal therapy. *Biomaterials* **2012**, *33*, 2961–2970, doi:10.1016/J.BIOMATERIALS.2011.12.052.
104. Lim, J.H.; Kim, D.E.; Kim, E.-J.; Ahrberg, C.D.; Chung, B.G. Functional Graphene Oxide-Based Nanosheets for Photothermal Therapy. *Macromol. Res. 2018 266* **2018**, *26*, 557–565, doi:10.1007/S13233-018-6067-3.
105. Huang, C.; Hu, X.; Hou, Z.; Ji, J.; Li, Z.; Luan, Y. Tailored graphene oxide-doxorubicin nanovehicles via near-infrared dye-lactobionic acid conjugates for chemo-photothermal therapy. *J. Colloid Interface Sci.* **2019**, *545*, 172–183, doi:10.1016/J.JCIS.2019.03.019.
106. Tager, A.A.; Safronov, A.P.; Sharina, S. V.; Galaev, I.Y. Thermodynamic study of poly(N-vinyl caprolactam) hydration at temperatures close to lower critical solution temperature. *Colloid Polym. Sci. 1993 2719* **1993**, *271*, 868–872, doi:10.1007/BF00652769.
107. Srivastava, A.; Kumar, A. Thermoresponsive poly(N-vinylcaprolactam) cryogels: Synthesis and its biophysical evaluation for tissue engineering applications. *J. Mater. Sci. Mater. Med.* **2010**, *21*, 2937–2945, doi:10.1007/s10856-010-4124-3.
108. Kou, Y.; Wang, S.; Luo, J.; Sun, K.; Zhang, J.; Tan, Z.; Shi, Q. Thermal analysis and heat capacity study of polyethylene glycol (PEG) phase change materials for thermal energy storage applications. *J. Chem. Thermodyn.* **2019**, *128*, 259–274, doi:10.1016/J.JCT.2018.08.031.
109. Cao, X.T.; Showkat, A.M.; Kang, I.; Gal, Y.S.; Lim, K.T. Beta-Cyclodextrin Multi-Conjugated Magnetic Graphene Oxide as a Nano-Adsorbent for Methylene Blue Removal. *J. Nanosci. Nanotechnol.* **2016**, *16*, 1521–1525, doi:10.1166/JNN.2016.11987.
110. Amiri, A.; Baghayeri, M.; Sedighi, M. Magnetic solid-phase extraction of polycyclic aromatic hydrocarbons using a graphene oxide/Fe3O4@polystyrene nanocomposite. *Microchim. Acta* **2018**, *185*, 1–9, doi:10.1007/S00604-018-2928-X/TABLES/3.
111. Yougbaré, S.; Mutalik, C.; Krisnawati, D.I.; Kristanto, H.; Jazidie, A.; Nuh, M.; Cheng, T.M.; Kuo, T.R. Nanomaterials for the Photothermal Killing of Bacteria. *Nanomater. 2020, Vol. 10, Page 1123* **2020**, *10*, 1123, doi:10.3390/NANO10061123.
112. Ma, G.; Qi, J.; Cui, Q.; Bao, X.; Gao, D.; Xing, C. Graphene Oxide Composite for Selective Recognition, Capturing, Photothermal Killing of Bacteria over Mammalian Cells. *Polym. 2020, Vol. 12, Page 1116* **2020**, *12*, 1116, doi:10.3390/POLYM12051116.
113. Liu, Z.; Zhao, X.; Yu, B.; Zhao, N.; Zhang, C.; Xu, F.J. Rough Carbon-Iron Oxide Nanohybrids for Near-Infrared-II Light-Responsive Synergistic Antibacterial Therapy. *ACS Nano* **2021**, *15*, 7482–7490,

doi:10.1021/ACSNANO.1C00894/SUPPL_FILE/NN1C00894_SI_001.PDF.

114. Ren, Y.; Liu, H.; Liu, X.; Zheng, Y.; Li, Z.; Li, C.; Yeung, K.W.K.; Zhu, S.; Liang, Y.; Cui, Z.; et al. Photoresponsive Materials for Antibacterial Applications. *Cell Reports Phys. Sci.* **2020**, *1*, 100245, doi:10.1016/J.XCRP.2020.100245.

115. Huo, J.; Jia, Q.; Huang, H.; Zhang, J.; Li, P.; Dong, X.; Huang, W. Emerging photothermal-derived multimodal synergistic therapy in combating bacterial infections. *Chem. Soc. Rev.* **2021**, *50*, 8762–8789, doi:10.1039/D1CS00074H.

116. Katalinić, I.; Budimir, A.; Bošnjak, Z.; Jakovljević, S.; Anić, I. The photo-activated and photo-thermal effect of the 445/970 nm diode laser on the mixed biofilm inside root canals of human teeth in vitro: A pilot study. *Photodiagnosis Photodyn. Ther.* **2019**, *26*, 277–283, doi:10.1016/J.PDPDT.2019.04.014.

117. Mahdavi, M.; Ahmad, M. Bin; Haron, M.J.; Namvar, F.; Nadi, B.; Ab Rahman, M.Z.; Amin, J. Synthesis, Surface Modification and Characterisation of Biocompatible Magnetic Iron Oxide Nanoparticles for Biomedical Applications. *Mol. 2013, Vol. 18, Pages 7533-7548* **2013**, *18*, 7533–7548, doi:10.3390/MOLECULES18077533.

118. Donadel, K.; Felisberto, M.D.V.; Fávere, V.T.; Rigoni, M.; Batistela, N.J.; Laranjeira, M.C.M. Synthesis and characterization of the iron oxide magnetic particles coated with chitosan biopolymer. *Mater. Sci. Eng. C* **2008**, *28*, 509–514, doi:10.1016/J.MSEC.2007.06.004.

119. Qu, J.; Liu, G.; Wang, Y.; Hong, R. Preparation of Fe3O4–chitosan nanoparticles used for hyperthermia. *Adv. Powder Technol.* **2010**, *21*, 461–467, doi:10.1016/J.APT.2010.01.008.